A global model of Love and Rayleigh surface wave dispersion and anisotropy, 25–250 s

Göran Ekström

Lamont-Doherty Earth Observatory of Columbia University, Palisades, NY 10964, USA. E-mail: ekstrom@ldeo.columbia.edu

SUMMARY

A large number of fundamental-mode Love and Rayleigh wave dispersion curves were determined from seismograms for 3330 earthquakes recorded on 258 globally distributed seismographic stations. The dispersion curves were sampled at periods between 25 and 250 s to determine propagation-phase anomalies with respect to a reference earth model. The data set of phase anomalies was first used to construct global isotropic phase-velocity maps at specific frequencies using spherical-spline basis functions with a nominal uniform resolution of 650 km. Azimuthal anisotropy was then included in the parametrization, and its importance for explaining the data explored. Only the addition of 2ζ azimuthal variations for Rayleigh waves was found to be resolved by the data. In the final stage of the analysis, the entire phase-anomaly data set was inverted to determine a global dispersion model for Love and Rayleigh waves parametrized horizontally using a spherical-spline basis, and with a set of B-splines to describe the slowness variations with respect to frequency. The new dispersion model, GDM52, can be used to calculate internally consistent global maps of phase and group velocity, as well as local and path-specific dispersion curves, between 25 and 250 s.

Key words: Surface waves and free oscillations; Seismic anisotropy; Seismic tomography.

GJI Seismology

1 INTRODUCTION

Love and Rayleigh surface waves are the most prominent phases on long-period seismograms recorded at regional and teleseismic distances, especially for shallow-focus earthquakes and explosions. In addition to their large amplitudes, these waves are characterized by laterally variable dispersion resulting from their sensitivity to Earth's shallow elastic structure, and especially the contrasting crustal and shallow-mantle structure of continents and oceans. Although early surface wave studies focused on characterizing dispersion along specific paths or across structurally homogeneous regions (e.g. Oliver 1962), the deployment of global and digital seismographic networks starting in the 1970s and 1980s led to the development of new techniques for characterizing long-period surface wave propagation globally (e.g. Masters *et al.* 1982; Nakanishi & Anderson 1982, 1983, 1984; Woodhouse & Dziewonski 1984; Tanimoto 1985; Tanimoto & Anderson 1985; Nataf *et al.* 1986; Wong 1989; Montagner & Tanimoto 1990, 1991). In the 1990s, progress was achieved through the accumulation of large data sets, and the development of new methods for measuring the dispersion of shorter period surface waves (e.g. Trampert & Woodhouse 1995b, 1996; Laske & Masters 1996; Zhang & Lay 1996; Ekström *et al.* 1997; van Heijst & Woodhouse 1999; Yoshizawa & Kennett 2002). The two-dimensional mapping of surface wave group and phase velocities is now a standard tool for investigating the laterally varying internal elastic structure of the crust and shal-

low mantle, with surface wave velocities at different periods providing complementary integral constraints on radial elastic structure.

Complicating efforts to improve the lateral resolution and fidelity of mapped phase velocities on global and regional scales are the anisotropic properties of crust and upper-mantle rocks, which produce azimuthal variations in surface wave phase velocities. These effects were documented first by Forsyth (1975), who demonstrated the existence of azimuthal variations of Rayleigh wave phase velocities across the Pacific Plate. Several other early studies mapped lateral variations of azimuthal anisotropy on regional (e.g. Montagner & Jobert 1988; Nishimura & Forsyth 1988) and global (e.g. Tanimoto & Anderson 1984, 1985; Montagner & Tanimoto 1990) scales. Recently, several authors have used large, modern data sets to develop models of anisotropic heterogeneity (e.g. Ekström 2000; Montagner & Guillot 2000; Trampert & Woodhouse 2003; Debayle *et al.* 2005; Beucler & Montagner 2006; Visser *et al.* 2008). Observations of azimuthal anisotropy are of value in part because they help constrain the elastic fabric of mantle materials, and thereby the deformation history and dynamic processes active in the upper mantle. Some agreement has been documented between seismological surface wave results and predictions based on geodynamic models of mantle flow and anisotropic fabric formation (e.g. Becker *et al.* 2003, 2007; Gaboret *et al.* 2003). Among seismological models, there is, however, still a lack of consensus on the pattern and strength of anisotropy, mainly as a result of the trade-off between isotropic and anisotropic heterogeneity.

An additional mapping challenge arises from the complexities of wave propagation, which become more evident as shorter period waves are investigated and attempts are made to determine lateral variations on shorter length scales. The benefits of including wave refraction, Fresnel zone or scattering effects in the mapping of observed surface wave dispersion to 2-D phase-velocity maps and 3-D intrinsic elastic properties have been stressed in a number of recent publications (e.g. Spetzler *et al.* 2002; Yoshizawa & Kennett 2002; Zhou *et al.* 2005). The extent to which the inclusion of finite-frequency effects in the interpretation of surface wave dispersion data influences the derived models on global and regional scales is not easily determined, however. The incremental advantage over a geometric ray-based approach afforded by, for example, a 2-D or 3-D scattering approach may be secondary to the effect on the solution of parametrization and regularization choices in the inverse problem (e.g. Boschi 2006; Trampert & Spetzler 2006; Ritsema *et al.* 2010).

Although most research interest in isotropic and anisotropic variations of surface wave phase velocities stems from the information these variations carry about intrinsic elastic properties of the Earth, path-specific dispersion curves and maps of surface wave velocities are also important for studies of earthquake focal mechanisms, as the propagation phase has to be predicted in order for the source phase to be determined correctly. For example, it was only following the development of intermediate-period phase-velocity maps for Love and Rayleigh waves (Ekström *et al.* 1997) that these waves could be included in the routine determination of centroid-moment tensors (CMTs) in the Global CMT project (Dziewonski *et al.* 1981; Arvidsson & Ekström 1998; Ekström *et al.* 2005). Similarly, accurate prediction of propagation phase is important for efforts to detect and locate seismic events using surface waves (Ekström 2006a). For these types of applications, the geographical details of the derived phase-velocity maps are secondary to the ability to predict the point-to-point propagation effects.

The first objective of this paper is the development and presentation of a large data set of surface wave phase-delay measurements and the analysis of these data in terms of isotropic phase-velocity maps. This initial investigation is in part a continuation of the work of Ekström *et al.* (1997) (hereafter referred to as ETL97), as similar measurement tools are employed here. Compared to the earlier study, the new developments and results presented here include (1) a significantly larger data set, (2) a broader period range (25–250 s) compared to the earlier study (35–150 s) and (3) a spherical-spline parametrization of the global maps.

The second objective is the determination of phase-velocity maps that incorporate azimuthal anisotropy, and an investigation of the ability of the new data set to resolve anisotropy of varying levels of complexity on a global scale. Previous work (e.g. Trampert & Woodhouse 2003) has addressed the statistical resolvability of additional anisotropic parameters in global phase-velocity inversions. Here, in a complementary approach, two experiments are presented that address the physical plausibility of the determined anisotropic structures.

The third objective is the derivation of a continuous dispersion model for Love and Rayleigh waves, designed to obviate the current need to interpolate phase-velocity maps at different periods to determine path-specific dispersion curves, and to add the possibility of predicting group and phase velocity simultaneously and consistently from the same dispersion model. For this purpose, a dispersion model fills the same role as a 3-D earth model, which can also be used to predict local surface wave phase and group velocities. In terms of the complexity of the required analysis, the direct determination of a global dispersion model is significantly simpler

than the determination of 3-D Earth structure. In particular, the non-unique and non-linear relationship between the phase velocity and the radial velocity profile is avoided, and no specific parametrization choices are needed with respect to, for example, crustal thickness and structure or the source region of intrinsic anisotropy.

The scope of this paper is deliberately limited. In particular, ray theory is used in the derivation of the models, and the potential limitations of this approach are not explored in this contribution. Future investigations may find the surface wave traveltime data set published here useful in deriving other models that incorporate more sophisticated theory in the analysis. The current contribution does not explore to any significant extent the implications of the derived dispersion curves for Earth structure. Natural continuations of this work are a comparison of dispersion predicted from published 3-D Earth models with the dispersion models presented here, determination of a 3-D anisotropic Earth model consistent with the dispersion models and incorporation of the dispersion models in CMT and surface wave earthquake-detection algorithms. These topics will be pursued in future work.

2 THEORY

The propagation of fundamental-mode Love and Rayleigh waves can be described using ray theory on a sphere (e.g. Tromp & Dahlen 1992, 1993). The surface wave seismogram $u(\omega)$ is written

$$u(\omega) = A(\omega) \exp[i \Phi(\omega)], \tag{1}$$

where $A(\omega)$ and $\Phi(\omega)$ are the amplitude and phase, respectively, of the wave as functions of angular frequency ω. For a given source–receiver geometry, the phase Φ is the sum of four terms

$$\Phi = \Phi_S + \Phi_R + \Phi_C + \Phi_P, \tag{2}$$

where Φ_S is the source phase calculated from the earthquake focal mechanism and geometrical ray take-off azimuth, Φ_R is the receiver phase, Φ_C is the static phase contribution from each ray focus and Φ_P is the propagation phase

$$\Phi_P(\omega) = \int \frac{\omega}{c(\omega)} \mathrm{d}s = \int \omega p(\omega) \, \mathrm{d}s, \tag{3}$$

where c is the local phase velocity and p is its reciprocal, the phase slowness. The integration follows the ray path. The amplitude A can be expressed as

$$A = A_S A_R A_\Delta A_Q, \tag{4}$$

where A_S is the magnitude of the excitation at the source, A_R is the receiver amplitude, A_Δ is the geometrical spreading factor and A_Q is the decay factor due to attenuation along the ray path. When the location and focal mechanism of the earthquake are known, a theoretical reference seismogram $u^0(\omega)$ based on a spherical earth model can be calculated and written as

$$u^0(\omega) = A^0(\omega) \exp[i \Phi^0(\omega)]. \tag{5}$$

The propagation phase for the reference surface wave is

$$\Phi_P^0(\omega) = \frac{\omega R \Delta}{c^0} = \omega R \Delta p^0 = \omega X p^0 \tag{6}$$

where c^0 is the spherical Earth phase velocity, p^0 is the spherical Earth phase slowness, Δ is the angular epicentral distance, R is the radius of the Earth and X is the propagation path length measured along the great circle. The observed surface wave $u(\omega)$

can be expressed as a perturbation with respect to the reference seismogram

$$u(\omega) = [A^0(\omega) + \delta A(\omega)] \exp i [\Phi^0(\omega) + \delta\Phi(\omega)]. \tag{7}$$

Assuming the source, receiver and ray-focus contributions to be known, the phase anomaly $\delta\Phi$ can be attributed to a perturbation in the propagation phase

$$\Phi_P = \Phi_P^0 + \delta\Phi = \frac{\omega X}{(c^0 + \overline{\delta c})}, \tag{8}$$

where $\overline{\delta c}$ is the apparent average phase-velocity perturbation, calculated for the distance X along the great circle.

Using ray theory, observations of phase anomalies can be interpreted as having accumulated along the path between a source at (θ_S, φ_S) and a receiver at (θ_R, φ_R)

$$\delta\Phi = \omega \int_{(\theta_S,\varphi_S)}^{(\theta_R,\varphi_R)} \delta p(\theta, \varphi)\,ds, \tag{9}$$

where $\delta p(\theta, \varphi)$ is the local phase-slowness perturbation. Since relative slowness variations ($\delta p / p^0$) for Love and Rayleigh waves in the period range analyzed in this paper can be larger than 20 per cent, we avoid making the approximation $1/(1 + \delta c/c^0) \approx 1 - \delta c/c^0$, which is otherwise commonly used to linearize the tomographic problem with respect to small perturbations $\delta c(\theta, \varphi)$ in local phase velocity. When, in the following, we present and discuss results in terms of relative velocity variations ($\delta c/c^0$), as is the common practice, these variations are calculated from the slowness variations by

$$\frac{\delta c}{c^0} = \frac{-\delta p}{p^0 + \delta p}. \tag{10}$$

The group slowness $g(\omega)$ is the inverse of the group velocity $U(\omega)$ and is related to the phase slowness by

$$g(\omega) = p(\omega) + \omega \frac{dp}{d\omega}(\omega). \tag{11}$$

The group slowness perturbation $\delta g(\omega)$ with respect to a spherical Earth's reference value $g^0(\omega)$ is then

$$\delta g(\omega) = \delta p(\omega) + \omega \frac{d(\delta p)}{d\omega}(\omega). \tag{12}$$

3 MEASUREMENT TECHNIQUE AND DATA COLLECTION

We used the algorithm described in ETL97 to collect phase-anomaly measurements. The method is based on phase-matched filtering and minimization of residual dispersion between an observed seismogram and a synthetic fundamental-mode surface wave seismogram. The dispersion and amplitude of the synthetic waveform are iteratively modified until the residual dispersion and the misfit between the observed and synthetic waveforms are minimized. The end result, for each measured Love and Rayleigh wave seismogram, is a smoothly varying perturbation in amplitude $\delta A(\omega)$ and apparent phase velocity $\overline{\delta c}(\omega)$ valid for a range of periods, as well as parameters quantifying the quality of the measurement. Fig. 1 shows an example of the waveform fitting and the resulting dispersion curve and frequency-dependent amplitude correction. Phase anomalies $\delta\Phi$ are obtained from the dispersion curves by evaluation at discrete periods. For a detailed description of the method, see ETL97.
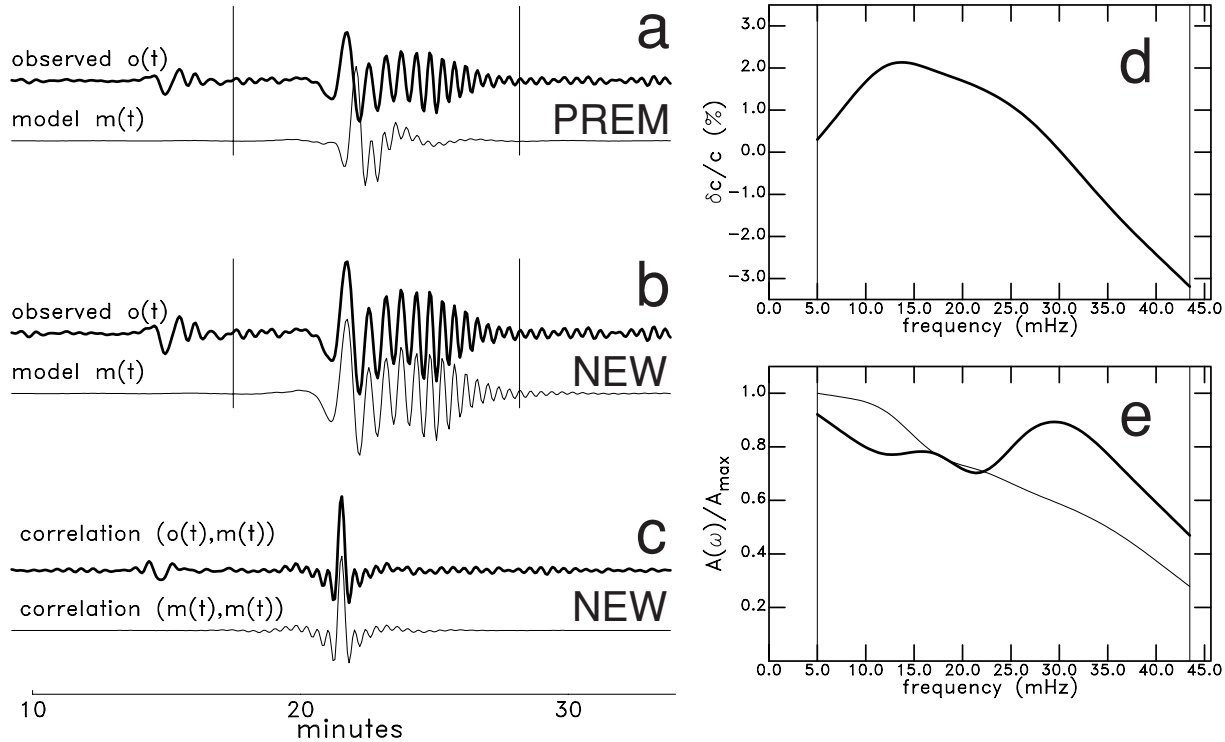
Figure 1. (a) Comparison of an observed seismogram and the corresponding synthetic waveform calculated for the PREM model (Dziewonski & Anderson 1981) before adjusting the fundamental-mode phase and amplitude. Thin vertical lines correspond to group velocities of 4.8 and 3.0 km s^{-1}. (b) Seismogram comparison after adjustments. (c) Correlation of observed and model seismograms, and autocorrelation of the model seismogram. (d) Derived phase-velocity perturbation (deviation from PREM) as a function of frequency. The shortest period considered is 23 s. (e) Derived amplitude (thick line) compared with PREM prediction (thin line).

We applied the measurement algorithm to seismograms recorded on globally distributed seismic stations. Specifically, we used data recorded on the Global Seismographic Network (network codes II and IU), the Chinese Digital Seismograph Network (CD and IC), the Mednet (MN), Geoscope (G), Geofon (GE) and Caribbean (CU) Networks, the Global Telemetered Seismograph Network (GT) and on selected stations of the Canadian National Seismograph Network (CN). We considered earthquake sources from 2000 to 2009, and used CMTs and centroid locations extracted from the Global CMT catalogue (Dziewonski *et al.* 1981; Ekström *et al.* 2005) in the calculation of synthetic seismograms. Only shallow sources ($h < 50$ km) were included to ensure that the fundamental-mode surface waves were the dominant long-period phase in the seismograms.

Two different sets of measurements were made. First, to accumulate a large data set of minor-arc shorter period measurements, analysis was attempted for earthquakes with $M_W \geq 5.5$. Variations in phase velocity and amplitude between 23 and 200 s were parametrized using eight spline basis functions equally spaced in frequency. To obtain a high-quality long-period set of dispersion curves, a second set of measurements including both minor- and major-arc arrivals (R1, R2; G1, G2) was collected using earthquakes with $M_W \geq 6.5$ and parametrizing phase velocity and amplitude using four spline basis functions between 105 and 400 s. The first set of measurements was subsequently used to constrain phase velocities for periods 125 s and shorter; the second set to constrain phase velocities for periods 150 s and longer.

Rayleigh wave dispersion was determined from the vertical component seismograms and Love wave dispersion from transverse seismograms constructed by rotation of the horizontal components using the great-circle back azimuth. Nearly one million earthquake–receiver paths were analyzed, but only a fraction of these yielded useful measurements. In particular, many of the smaller earthquakes were recorded with high signal-to-noise ratios only at the quietest stations.

For the shorter period set of measurements, dispersion curves were first determined between 200 and 50 s, then between 200 and 32 s and finally between 200 and 23 s. As the short-period limit of the analysis is extended, fewer paths yield acceptable dispersion curves, in part due to complexities of wave propagation not matched by the model seismograms. For the minor- and major-arc measurements at long periods, a single dispersion curve was determined between 400 and 105 s. The dispersion curves were subsequently evaluated to determine phase anomalies at specific periods. To identify acceptable measurements, we used the same selection criteria as in ETL97. Acceptable measurements were determined to be of quality A, B or C, depending on the values of the fitting parameters. The total number of phase anomalies collected at each period is shown in Table 1. The jumps in the number of observations seen between 30 and 32 s, 45 and 50 s and 125 and 150 s result from the data being derived from different sets of dispersion curves.

Fig. 2 shows the locations of earthquakes and stations that contributed at least one observation to this study. Although the geographical distribution of earthquakes is similar to that in ETL97, this study includes many stations in new locations, notably several in the Pacific Ocean Basin. Large areas in the southern oceans still lack good station coverage. Fig. 3 shows the rms of the phase anomalies after removing a global average phase-velocity contribution at each period. The phase-anomaly signal strength increases roughly as the square of the frequency and is approximately three full cycles for both Love and Rayleigh waves at 25 s.

Table 1. The number of phase anomalies at each period. The reduced number N_r refers to the effective number of data following the weighting that accounts for uneven spatial sampling.

Period	N (Love)	N_r (Love)	N (Rayleigh)	N_r (Rayleigh)
25	18 670	8308	103 633	36 109
27	19 034	8420	104 820	36 366
30	19 187	8465	105 796	36 592
32	35 858	14 558	178 997	54 253
35	35 935	14 578	179 296	54 313
40	35 977	14 591	179 657	54 369
45	36 022	14 607	179 802	54 404
50	82 958	30 822	282 579	72 488
60	85 646	31 640	286 132	72 970
75	85 742	31 674	286 302	72 972
100	83 463	31 199	282 996	72 565
125	62 829	25 668	247 410	65 826
150[a]	43 999	25 025	83 093	39 123
200[a]	30 870	19 170	82 518	38 892
250[a]	36 991	21 563	78 291	37 172

[a]For periods 150 s and longer, the numbers reflect minor- and major-arc data.

3.1 Data errors and uncertainties

Errors in the measured phase anomalies arise from several sources. These include (1) error in the source location, (2) error in the CMT focal mechanism, (3) error in the source excitation, caused by an inappropriate source depth or the assumed local structure, (4) interference of the fundamental mode with other phases in the seismogram, (5) errors in the instrument-response function and (6) measurement errors caused by seismic noise. Following ETL97, we estimated observational uncertainties for the phase anomalies by comparing measurements for similar paths. Table 2 gives the values for A-, B- and C-quality observations. Fig. 4 shows the estimated uncertainty for quality-A observations as a function of frequency, indicating a roughly linear increase in the phase uncertainty with respect to frequency. This trend is consistent with an error related to the epicentral distance, as suggested by the lines in Fig. 4, which illustrate the phase error that would be introduced by a source mislocation of 15 km in the direction to or from the station. Smith & Ekström (1997) estimated that CMT centroid locations deviate from true earthquake locations by approximately 25 km on average, which indicates that source mislocation is likely to be an important contributor to the data errors.

It is likely, however, that the empirical uncertainty is an underestimate of the true uncertainty. Errors associated with regional bias in source locations (e.g. Engdahl *et al.* 1982; Smith & Ekström 1996; Yang *et al.* 2004) will not contribute to uncertainty estimates based on similar paths, for example. Other types of errors, such as those associated with the instrument response, also will not contribute, when measurements at the same station are compared. However, the estimated uncertainties reflect the combined effects of several of the error sources, and allow us to interpret and model the observations with quantitative consideration of quality-of-fit parameters.

An additional source of error and uncertainty is associated with the underlying assumption of the measurement technique that the seismic signal contains a smoothly dispersed fundamental-mode surface wave for which it is possible to measure a meaningful phase and amplitude. Even for a simple and smooth velocity structure, this assumption can be violated for near-nodal take-off angles and for paths that generate multipathing and diffraction. Seismograms that suffer such complications are unlikely to be fit well by the synthetic
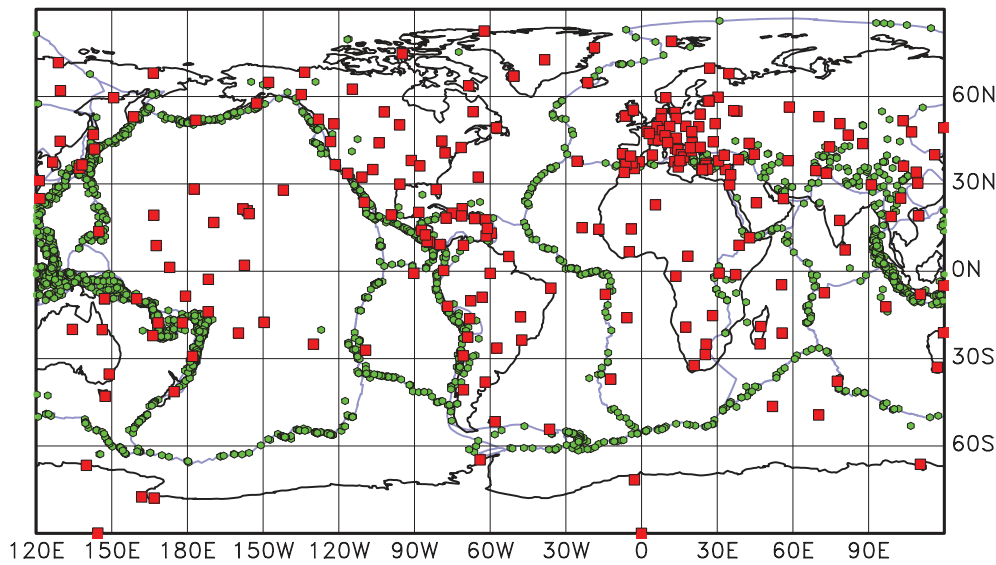
Figure 2. Global map showing the locations of 3330 earthquakes (hexagons) and 258 stations (squares) that contributed to the analysis. Plate boundaries (Bird 2003) are shown in light blue.
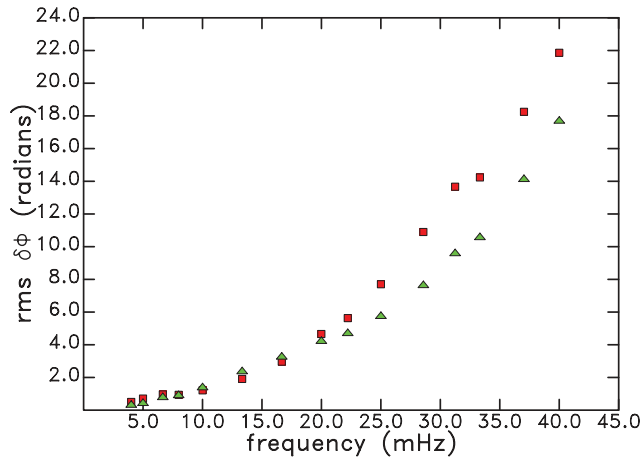

Figure 3. The rms phase-anomaly signal for (squares) Love and (triangles) Rayleigh waves at different frequencies.

Table 2. Empirical uncertainties (radians) estimated from pairwise similar paths.

Period	Love waves			Rayleigh waves		
	σ_A	σ_B	σ_C	σ_A	σ_B	σ_C
25	0.903	1.654	3.130	0.951	1.778	3.824
27	0.757	1.199	1.939	0.833	1.248	2.284
30	0.589	0.860	1.261	0.709	0.963	1.525
32	0.595	0.956	1.532	0.759	1.247	2.181
35	0.477	0.677	1.086	0.648	0.987	1.748
40	0.385	0.509	0.759	0.533	0.769	1.298
45	0.338	0.430	0.595	0.454	0.643	1.033
50	0.403	0.655	0.988	0.569	1.038	1.771
60	0.319	0.503	0.690	0.437	0.749	1.220
75	0.262	0.406	0.519	0.331	0.528	0.792
100	0.215	0.350	0.411	0.250	0.393	0.544
125	0.226	0.357	0.366	0.226	0.348	0.401
150[a]	0.122	0.224	0.410	0.146	0.216	0.394
200[a]	0.099	0.212	0.351	0.106	0.167	0.262
250[a]	0.117	0.256	0.272	0.106	0.179	0.252

[a]For periods 150 s and longer, the numbers reflect minor- and major-arc data.

waveform used in the measurement algorithm, and are therefore also unlikely to yield dispersion curves of acceptable quality. The removal of low-quality measurements is an important step in reducing the overall observational uncertainties in the data set.

4 PHASE-VELOCITY MAPS

4.1 The forward problem

In Section 2, we made use of ray theory to describe the propagation phase of a fundamental-mode surface wave seismogram, and to define the phase anomaly $\delta\Phi$. Our measurement method is, however, not strictly dependent on the validity of ray theory and, to the extent that part of the wavefield can be represented by a surface wave with smooth dispersion, the measured phase anomalies can be interpreted using any appropriate theory. With ray theory, we can use eq. (9) to interpret the observed phase anomaly; with 2-D wave-propagation theories (e.g. Born scattering) we would instead write

$$\delta\Phi = \omega \int_\Omega K^{2D}(\theta, \varphi)\delta p(\theta, \varphi)\, d\Omega, \qquad (13)$$

where $K^{2D}(\theta, \varphi)$ is an appropriate phase-slowness sensitivity function (e.g. Spetzler *et al.* 2002) defined across the surface Ω of the Earth. 3-D theoretical expressions lead to a relationship

$$\delta\Phi = \omega \sum_{i=1}^{N} \left\{ \int_V K_i^{3D}(\theta, \varphi, \mathbf{r})\delta\xi_i(\theta, \varphi, \mathbf{r})\, dV \right\}, \qquad (14)$$

where $K_i^{3D}(\theta, \varphi, \mathbf{r})$ is the appropriate sensitivity function for the phase anomaly $\delta\Phi$ and the ith of N intrinsic 3-D variables ξ_i (e.g. *S*-wave velocity, *P*-wave velocity and density) defined throughout the volume V of the Earth's interior (e.g. Zhou *et al.* 2004).

Higher order theories, such as scattering theory, describe how the wavefield (not the phase) is modified by perturbations in the structure. Since, in practice, $\delta\Phi$ is a measurement of the wavefield obtained using a particular technique, the specific form of the sensitivity functions $K^{2D}(\theta, \varphi)$ and $K_i^{3D}(\theta, \varphi, \mathbf{r})$ will also depend on the measurement technique (Dahlen *et al.* 2000; Zhou *et al.* 2004). In general, higher order sensitivity functions also depend on the
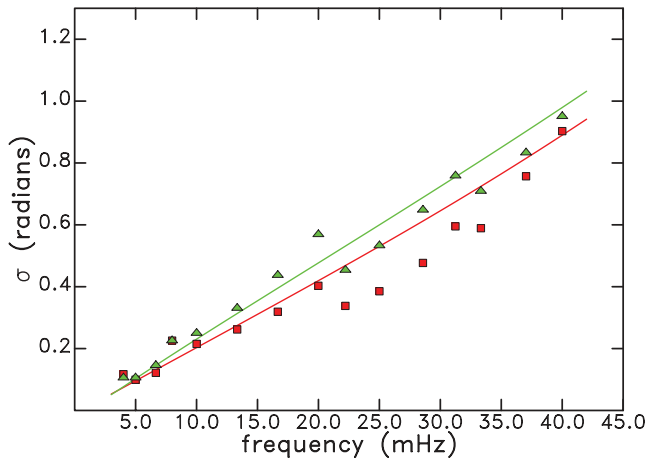
Figure 4. Estimates of observational uncertainties for (squares) Love and (triangles) Rayleigh waves based on observations from pairwise similar paths. The lines show the phase error that would result from an error in epicentral distance of 15 km, assuming PREM phase velocities.

earthquake focal mechanism. Here, we use surface wave ray theory and great-circle paths in our analysis of the phase-anomaly data set; with appropriate developments, the measurements could be interpreted within other theoretical frameworks.

4.2 Model parametrization

To formulate an inverse problem of finite dimensions based on the relationship between phase anomalies and laterally varying velocities, the laterally varying slowness perturbation $\delta p(\theta, \varphi)/p^0$ at a given period can be parametrized in terms of a set of basis functions on the surface of the sphere

$$\frac{\delta p(\theta, \varphi)}{p^0} = \sum_{i=1}^{N} a_i B_i(\theta, \varphi), \tag{15}$$

where $B_i(\theta, \varphi)$ is a basis function, such as a latitude–longitude pixel, a spherical spline or a single spherical harmonic, a_i is a model coefficient and N is the total number of basis functions used in the representation. Here, we use a spherical-spline parametrization. The basis functions are centred on N knot points $i = 1, 2, \ldots, N$ distributed across the surface of the Earth, to provide either uniform or variable resolution. The value $f_i(\theta, \varphi)$ of each basis function i depends on the distance Δ from the ith knot point

$$f_i = \begin{cases} \frac{3}{4}\left(\Delta/\Delta_i^0\right)^3 - \frac{3}{2}\left(\Delta/\Delta_i^0\right)^2 + 1, \\ \qquad\qquad\qquad\qquad \Delta \leq \Delta_i^0 \\ -\frac{1}{4}\left(\Delta/\Delta_i^0\right)^3 + \frac{3}{2}\left(\Delta/\Delta_i^0\right)^2 - 3(\Delta/\Delta_i^0) + 2, \\ \qquad\qquad\qquad\qquad \Delta_i^0 \leq \Delta \leq 2\Delta_i^0, \end{cases} \tag{16}$$

where $2\Delta_i^0$ is the full range of the ith spline basis function. When the knot points are distributed nearly uniformly across the Earth's surface according to the tessellation scheme described by Wang & Dahlen (1995), Δ_i^0 is chosen to be the average distance between knot points. This is the approach we use here. The geographical distribution of isotropic phase-slowness perturbations is then written

$$\frac{\delta p(\theta, \varphi)}{p^0} = \sum_{i=1}^{N} u_i f_i(\theta, \varphi), \tag{17}$$

where u_i are the model coefficients.

Smith & Dahlen (1973) showed that, in the case of a weakly anisotropic Earth, the azimuthal variations in Love and Rayleigh wave velocities can be described by patterns having simple twofold and fourfold azimuthal symmetry with respect to the propagation azimuth ζ. We use this result to write

$$p^\star(\zeta) = p^0\left(1 + \frac{\delta p}{p^0} + A\,\cos 2\zeta + B\,\sin 2\zeta \right.$$
$$\left. + C\,\cos 4\zeta + D\,\sin 4\zeta\right), \tag{18}$$

where $p^\star(\zeta)$ is the azimuthally varying phase slowness and A, B, C and D are coefficients describing azimuthal variations in phase slowness with respect to the reference isotropic slowness p^0. The azimuth ζ is measured with respect to the local meridian.

To describe lateral variations in velocity, including variations in anisotropic properties, we write

$$\frac{\delta p^\star(\theta, \varphi; \zeta)}{p^0} = \frac{\delta p(\theta, \varphi)}{p^0} + A(\theta, \varphi)\,\cos 2\zeta + B(\theta, \varphi)\,\sin 2\zeta$$
$$+ C(\theta, \varphi)\,\cos 4\zeta + D(\theta, \varphi)\,\sin 4\zeta. \tag{19}$$

The laterally varying coefficients $A(\theta, \varphi)$, $B(\theta, \varphi)$, $C(\theta, \varphi)$ and $D(\theta, \varphi)$ can be expanded using some appropriate set of basis functions. For an expansion in spherical harmonics, generalized spherical harmonics are needed (e.g. Trampert & Woodhouse 1995a, 2003), as an expansion of the coefficients A, B, C and D in scalar spherical harmonics leads to singularities at the geographic poles, where constant azimuths ζ at nearby points do not correspond to parallel directions. An alternative method based on spherical splines (eq. 16) was described by Ekström (2006b), and is the one we adopt here. To make it possible to represent a smoothly varying direction in regions close to the poles, Ekström (2006b) introduced the concept of a 'local parallel azimuth' with which it is possible to write the spherical-spline representation of the phase-slowness variations

$$\frac{\delta p^\star(\theta, \varphi; \zeta)}{p^0} = \sum_{i=1}^{N} [u_i f_i(\theta, \varphi) + a_i f_i(\theta, \varphi)\,\cos 2\zeta_i$$
$$+ b_i f_i(\theta, \varphi)\sin 2\zeta_i + c_i f_i(\theta, \varphi)\,\cos 4\zeta_i + d_i f_i(\theta, \varphi)\,\sin 4\zeta_i], \tag{20}$$

where $\zeta_i(\theta, \varphi; \zeta)$ is the local parallel azimuth defined at the ith knot point. The local parallel azimuth is defined by

$$\zeta_i(\theta, \varphi; \zeta) = (\zeta(\theta, \varphi) - (\alpha_i(\theta, \varphi) - \beta_i(\theta, \varphi) - \pi)), \tag{21}$$

where α_i is the azimuth from (θ, φ) to the ith spline point and β_i is the back azimuth from the ith spline point to (θ, φ).

4.3 Data weighting

In the inverse tomographic problem, we wish to determine the model coefficients that best explain the set of observed phase anomalies. We form the misfit function to be minimized from the observed anomaly $\delta\Phi^{\text{obs.}}$ and the predicted anomaly $\delta\Phi^{\text{pred.}}$

$$\chi^2 = \sum_{j=1}^{N} \frac{w_j^2}{\sigma_j^2}\left(\delta\Phi_j^{\text{obs.}} - \delta\Phi_j^{\text{pred.}}\right)^2, \tag{22}$$

where j is the index of the observation, N is the total number of observations, σ_j is the observational uncertainty and w_j is a weight applied to the jth observation. Weighting is introduced to reduce the impact on the model of repeated observations of some particular paths. One such path is that leading from the many earthquakes in the Tonga–Kermadec subduction zone to the large number of stations in North America.

We implement the weighting in the following way. Starting with a set of 1442 evenly distributed gridpoints on the sphere we determine, for each earthquake–station path, the gridpoints closest to the earthquake and the station. The number of observations that share the same starting and ending gridpoints is designated N_P, and each observation corresponding to this path is assigned a weight

$$w_j = (1 + \log_{10} N_P)^{-1}. \tag{23}$$

This, for example, makes observations corresponding to a path sampled 10 times contribute to χ^2 only 2.5 times as much as an observation corresponding to a path sampled just once. The total number of effective observations is reduced by the weighting; Table 1 gives the reduced number of observations,

$$N_r = \sum_{j=1}^{N} w_j, \tag{24}$$

for Love and Rayleigh waves at each period.

4.4 Model estimation and regularization

When the number of observations is large in comparison with the number of parameters to be estimated, the inverse problem can be overdetermined and no regularization of the inverse problem is necessary. When regularization is necessary, this is introduced by minimizing the sum of χ^2 and some additional function that reflects the size or roughness of the phase-slowness model. We define the strength $\mathcal{S}$ of the isotropic phase slowness as the rms value of the variations

$$\mathcal{S} = \left[\frac{1}{4\pi} \int_\Omega \left(\frac{\delta p}{p^0} \right) \cdot \left(\frac{\delta p}{p^0} \right) \, d\Omega \right]^{1/2}, \tag{25}$$

and the roughness $\mathcal{R}$ as the rms gradient of the global isotropic phase-slowness variations

$$\mathcal{R} = \left[\frac{1}{4\pi} \int_\Omega \left(\nabla \frac{\delta p}{p^0} \right) \cdot \left(\nabla \frac{\delta p}{p^0} \right) \, d\Omega \right]^{1/2}. \tag{26}$$

Similarly, we define the anisotropic strengths $\mathcal{S}_{2\zeta}$ and $\mathcal{S}_{4\zeta}$, and roughnesses $\mathcal{R}_{2\zeta}$ and $\mathcal{R}_{2\zeta}$

$$\mathcal{S}_{n\zeta} = \left[\frac{1}{4\pi} \int_\Omega \left(s_{n\zeta}^2 + c_{n\zeta}^2 \right) \, d\Omega \right]^{1/2}, \tag{27}$$

and

$$\mathcal{R}_{n\zeta} = \left[\frac{1}{4\pi} \int_\Omega \left\{ (\nabla s_{n\zeta}) \cdot (\nabla s_{n\zeta}) + (\nabla c_{n\zeta}) \cdot (\nabla c_{n\zeta}) \right\} \, d\Omega \right]^{1/2}, \tag{28}$$

where $s_{n\zeta}$ and $c_{n\zeta}$ are the spatially varying sine and cosine coefficients of 2ζ and 4ζ anisotropy. In a full inversion for isotropic and 2ζ and 4ζ anisotropic phase-slowness variations, we then choose to minimize the quantity $\tilde{\chi}^2$, where

$$\tilde{\chi}^2 = \left(\chi^2 + \gamma \mathcal{R}^2 + \gamma_{2\zeta} \mathcal{R}_{2\zeta}^2 + \gamma_{4\zeta} \mathcal{R}_{4\zeta}^2 \right), \tag{29}$$

and γ, $\gamma_{2\zeta}$ and $\gamma_{4\zeta}$ are parameters that define the relative weights assigned to fitting the observations and to obtaining a smooth model. Solutions to the inverse problem are obtained using Cholesky factorization.

4.5 Isotropic inversions

At all periods, the phase-anomaly data are sufficient to constrain global isotropic slowness anomalies expanded on a spherical-spline basis with 362 nodes and an average node separation of 11.5° without imposing smoothness constraints. Only for Love waves at periods shorter than 32 s is there an indication of minor instability in the resulting models in poorly sampled areas, such as the southern oceans. The purpose of determining these coarse maps is to obtain baseline estimates of the strength of model anomalies, as well as reference quality-of-fit values for a simple model parametrization. Table 3 lists the residual normalized variance as well as the quality-of-fit estimate, for which we use χ^2/N_r. Although the models are smooth, they explain more than 90 per cent of the signal at many periods. This is a consequence of the path-averaging nature of traveltime data, as well as the dominance of long-wavelength anomalies in the velocity field, mainly owing to the sizes and shapes of oceanic and continental areas.

Fig. 5 shows the rms phase-slowness variations of the 362 spline models as a function of period. The rms strength of the anomalies shows some structure as a function of frequency, with rapid increases at higher frequencies. A change in slope occurs at around 15 mHz for Love waves and around 25 mHz for Rayleigh waves. As discussed in ETL97, the strong anomalies at shorter periods are highly spatially correlated with predicted anomalies based on a model of the Earth's crust.

4.5.1 High-resolution isotropic inversions

We next inverted the same data set for isotropic slowness variations using a spline basis with 1442 nodes and an average node separation of 5.7°. The nominal resolution for this parametrization is equivalent to an expansion in spherical harmonics to degree 38. Although we found that it is possible to invert the data without damping for the best and most extensive data sets (e.g. Rayleigh waves at 60 s), this was not true in general. In particular, the smaller data sets corresponding to short-period Love waves and the noisier very long period data sets required regularization to yield stable and meaningful inversion results.

The choice of the weighting parameter γ in eq. (29) typically requires subjective judgement in addition to assessment of objective variables. One reason for this is that the true errors in the data and in the theories used in the modelling of the data are partly unknown. These errors are also unlikely to be random, which makes standard statistical tools less useful. Many investigators have used the calculation and assessment of trade-off curves, aided by qualitative or quantitative evaluation of the resulting models, to determine the appropriate balance between fitting the data and obtaining meaningful and realistic models. This is also the approach we followed here.

For each data set, we minimized $\tilde{\chi}^2$ in eq. (29) repeatedly for different values of γ and examined the trade-off between the roughness $\mathcal{R}$ and the quality-of-fit χ^2/N_r. Fig. 6 shows examples for several periods. Typically, a range of solutions is acceptable at each period, but we found that it was not possible to find a single γ that resulted in acceptable models for all data sets. This is not unanticipated, given the variations in signal strength (Fig. 3) and observational uncertainties (Fig. 4) that exist between 25 and 250 s period. We found that at shorter periods, we needed a relatively smaller γ to obtain an acceptable model, and that by making γ vary inversely with respect to frequency

$$\gamma(f) = \frac{f_0}{f} \gamma(f_0), \tag{30}$$

where f is the frequency and f_0 is an arbitrary reference frequency (chosen to be 4 mHz), we were able to obtain acceptable models from all of the data sets.

Table 3. Residual normalized variance $v = \sum_{i=1}^{N}(\delta\Phi_i^{\text{obs.}} - \delta\Phi_i^{\text{pred.}})^2/\sum_{i=1}^{N}(\delta\Phi_i^{\text{obs.}})^2$, quality of fit χ^2/N_r, model strength $\mathcal{S}$ and roughness $\mathcal{R}/\mathcal{S}$ for the undamped 362-spline isotropic inversions and the damped 1442-spline isotropic inversions. The last four columns give the parameters corresponding to the phase-velocity maps predicted from the Love and Rayleigh dispersion models GDM52L and GDM52R. Maps predicted from GDM52R include 2ζ anisotropic variations. Only the isotropic part is included in the calculation of $\mathcal{S}$ and $\mathcal{R}$.

Period		Undamped Inversion				Damped Inversion				Dispersion Model GDM52			
		v	χ^2/N_r	$\mathcal{S}$	$\mathcal{R}/\mathcal{S}$	v	χ^2/N_r	$\mathcal{S}$	$\mathcal{R}/\mathcal{S}$	v	χ^2/N_r	$\mathcal{S}$	$\mathcal{R}/\mathcal{S}$
L	25	0.041	4.45	6.33	6.39	0.033	3.45	6.07	6.32	0.033	3.59	6.01	6.51
L	27	0.028	4.80	5.71	6.13	0.020	3.42	5.59	6.72	0.020	3.43	5.65	7.01
L	30	0.020	4.61	4.96	6.03	0.013	3.05	4.89	6.93	0.013	3.07	4.99	7.43
L	32	0.023	4.08	4.57	5.81	0.017	2.87	4.55	7.17	0.017	2.89	4.58	7.65
L	35	0.022	4.82	4.02	5.91	0.016	3.37	4.03	7.62	0.016	3.37	4.06	7.94
L	40	0.024	5.04	3.34	6.23	0.018	3.55	3.34	8.18	0.018	3.56	3.37	8.43
L	45	0.030	4.90	2.85	6.58	0.022	3.43	2.86	8.64	0.022	3.51	2.86	8.81
L	50	0.064	3.72	2.48	6.85	0.055	3.02	2.51	9.13	0.054	3.07	2.52	9.15
L	60	0.084	3.38	2.08	7.22	0.072	2.76	2.11	9.54	0.072	2.78	2.11	9.48
L	75	0.114	2.91	1.82	7.51	0.101	2.47	1.84	9.44	0.101	2.49	1.83	9.19
L	100	0.155	2.22	1.60	7.34	0.144	2.00	1.59	8.62	0.145	2.02	1.58	8.38
L	125	0.205	1.90	1.47	7.12	0.197	1.78	1.43	7.63	0.200	1.84	1.44	7.56
L	150[a]	0.229	3.37	1.36	6.35	0.222	3.16	1.36	7.87	0.224	3.24	1.33	7.01
L	200[a]	0.300	2.11	1.18	6.10	0.294	2.01	1.15	6.64	0.297	2.05	1.15	6.48
L	250[a]	0.422	2.12	1.03	6.17	0.416	2.06	0.99	6.24	0.417	2.08	1.00	6.32
R	25	0.060	4.42	4.37	5.62	0.049	3.32	4.52	8.39	0.048	3.19	4.43	7.63
R	27	0.042	4.58	3.86	5.84	0.031	3.22	4.00	8.81	0.029	2.99	3.97	8.28
R	30	0.038	4.27	3.24	6.19	0.026	2.87	3.37	9.20	0.024	2.57	3.33	8.63
R	32	0.055	3.15	2.90	6.34	0.044	2.32	3.01	9.10	0.040	2.09	2.99	8.81
R	35	0.060	3.29	2.57	6.72	0.047	2.40	2.68	9.66	0.043	2.11	2.64	9.13
R	40	0.065	3.38	2.23	7.19	0.051	2.47	2.34	10.28	0.045	2.12	2.28	9.61
R	45	0.067	3.43	2.05	7.40	0.052	2.53	2.17	10.56	0.045	2.14	2.09	9.56
R	50	0.120	2.51	1.97	7.30	0.108	2.08	2.05	10.01	0.099	1.81	2.00	9.27
R	60	0.111	2.62	1.86	7.27	0.100	2.19	1.94	9.89	0.089	1.86	1.88	8.88
R	75	0.102	2.53	1.72	7.24	0.092	2.13	1.78	9.73	0.077	1.72	1.72	8.38
R	100	0.135	2.10	1.40	7.16	0.126	1.86	1.44	9.54	0.107	1.51	1.39	8.08
R	125	0.202	1.89	1.14	7.10	0.194	1.75	1.16	9.30	0.173	1.55	1.12	7.83
R	150[a]	0.211	2.52	0.92	6.78	0.199	2.31	0.95	9.92	0.180	2.02	0.89	7.89
R	200[a]	0.319	2.23	0.67	6.49	0.309	2.10	0.70	9.99	0.293	1.94	0.66	8.63
R	250[a]	0.496	1.98	0.55	6.68	0.484	1.89	0.57	9.98	0.466	1.79	0.55	9.24

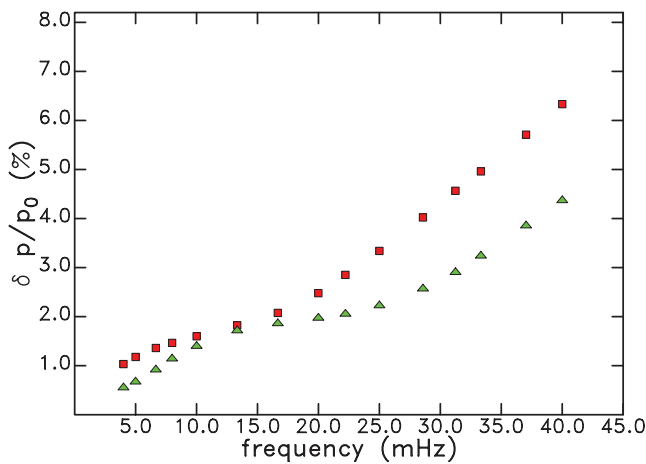[a]For periods 150 s and longer, the numbers reflect minor- and major-arc data.

Figure 5. Strength (rms) of the (squares) Love and (triangles) Rayleigh wave phase-slowness models at different frequencies. The results correspond to the undamped isotropic inversion using 362 spline functions to represent the laterally varying slownesses.
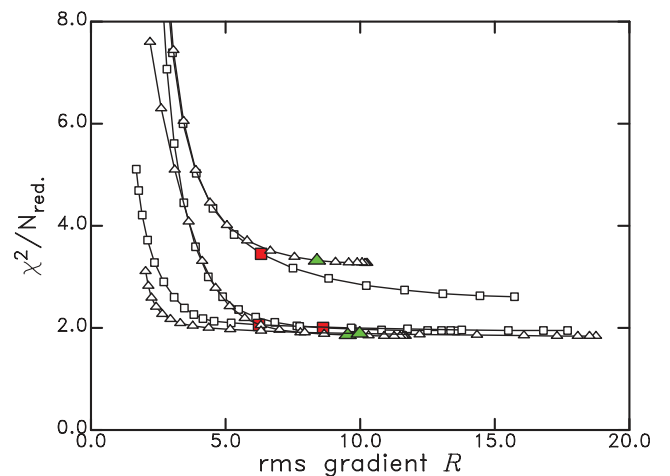

Figure 6. Trade-off curves for the high-resolution isotropic inversion for (squares) Love and (triangles) Rayleigh waves at 25, 100 and 250 s. The larger, filled symbols indicate the preferred inversion results.

Fig. 7 shows phase-velocity maps converted from the phase-slowness models of Love and Rayleigh waves at the longest and shortest periods considered in this study, 250 s and 25 s. The 250-second Rayleigh wave map has a strength $\mathcal{S} = 0.57$ per cent,

and a spherical harmonic degree-two pattern with slower velocities in the Pacific and Africa. At 250 s, the Love wave map is stronger ($\mathcal{S} = 0.99$ per cent), and the anomalies show a clear correlation with surface tectonics with fast velocities correlating with
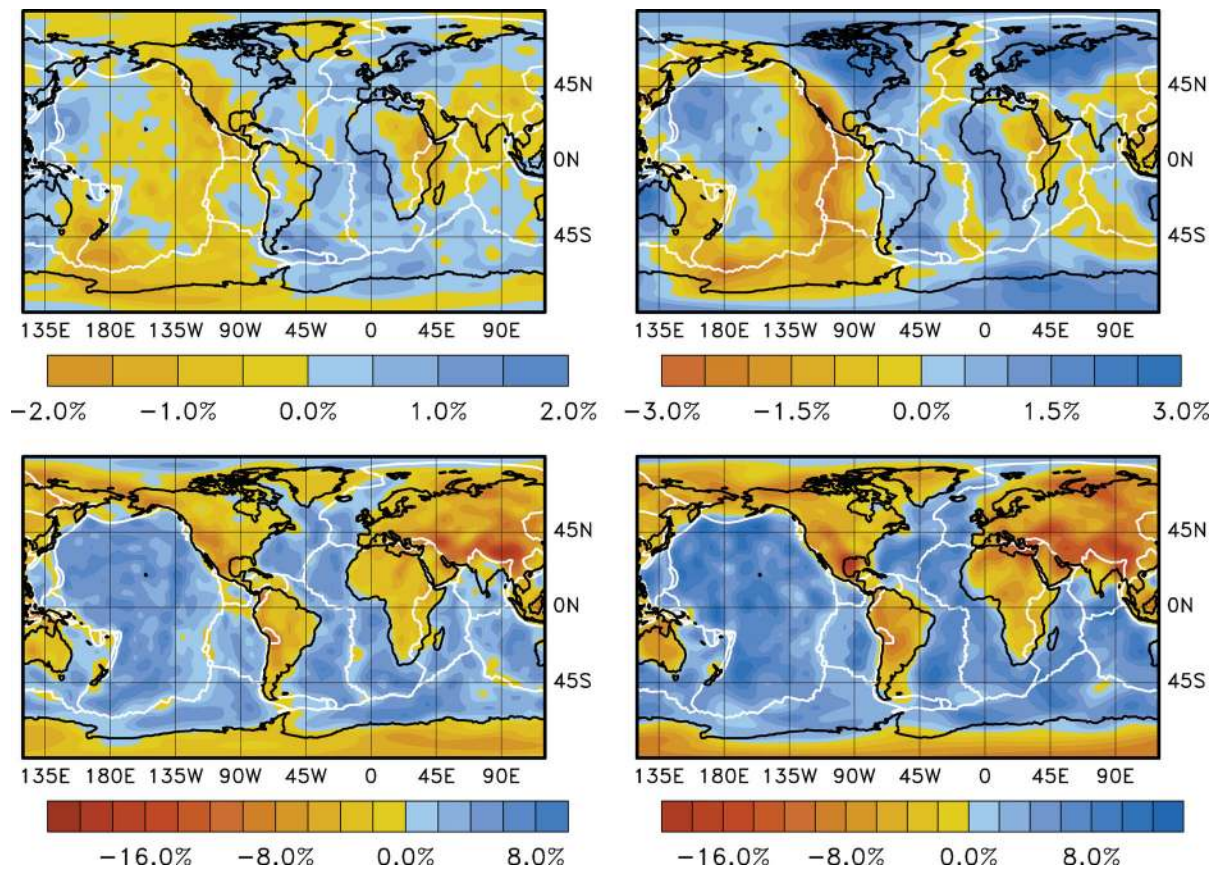
Figure 7. Maps of phase-velocity anomalies with respect to PREM resulting from the damped inversion of only isotropic variations. (Top left) Rayleigh waves at 250 s, (bottom left) Rayleigh waves at 25 s, (top right) Love waves at 250 s, (bottom right) Love waves at 25 s. Plate boundaries (Bird, 2003) are shown in white.

old seafloor age and the cratonic portions of the continents. The Love and Rayleigh wave maps at 25 s show a very clear correlation with the thickness of the crust and, for Love waves, the thickness of low-velocity sediments in deep basins such as the Gulf of Mexico. Considering the very large velocity anomalies in the short-period maps, and the large wave-refraction effects that they must cause, it is surprising that the inversion leads to such spatially well-defined anomalies.

The new results agree well with the phase-velocity maps developed in ETL97 across the period range spanned by the earlier study (35–150 s). This agreement is not surprising considering the similarities of the two studies, but it is still encouraging considering that the data sets are entirely independent. The spatial correlation of phase-velocity maps from the two studies is greater than 0.92 for 100 s and shorter periods, and smaller for 150 s (0.86 for Rayleigh waves and 0.91 for Love waves). The slightly worse correlation at 150 s may be related to the fact that ETL97 included only minor-arc data; in this study both minor and major-arc data are used at this period. In general, the new maps have stronger short-wavelength features than those of ETL97, especially in the Rayleigh wave maps. However, as discussed in the next section, some of these short-wavelength features are likely to be artefacts resulting from the omission of azimuthal anisotropy in this stage of the analysis.

4.6 Anisotropic inversions

It is well established that azimuthal anisotropy influences the propagation of intermediate-period Rayleigh waves (e.g. Forsyth 1975;

Nishimura & Forsyth 1988; Montagner & Tanimoto 1990), especially for waves traversing oceanic lithosphere. While much progress has been made in mapping anisotropic properties of the crust and upper mantle in recent years, key questions remain only partly answered. For example, regarding surface wave anisotropy, three open issues are (1) the fidelity with which azimuthal anisotropy can be imaged globally, (2) the nature and extent of trade-offs between isotropic and anisotropic structure and (3) the absolute magnitude of anisotropy. In addition, while most studies of surface wave anisotropy have investigated the 2ζ azimuthal variations in Rayleigh wave velocities, the 4ζ variations that are also predicted to exist (e.g. Montagner & Nataf 1986; Montagner & Anderson 1989) have been harder to detect and constrain. In studies that have found Love wave azimuthal anisotropy of any kind, the signal has been weaker than for Rayleigh waves, and less clearly correlated with any plausible fabric-generating geodynamic processes.

To investigate the extent to which azimuthal anisotropy can be constrained with the data sets collected in this study, we first performed a number of experiments using the Love and Rayleigh wave data sets at a period of 60 s. This period falls in the range where we have the largest number of good measurements, and the best global path coverage. In the experiments, we parametrized the model using the same 1442-node basis as in the high-resolution isotropic inversions. We started by imposing the same level of isotropic damping (γ) preferred in the isotropic inversions, and then varied $\gamma_{2\zeta}$ and $\gamma_{4\zeta}$, with $\gamma_{2\zeta} = \gamma_{4\zeta}$. Fig. 8 shows the maps that result when $\gamma_{2\zeta}$ and $\gamma_{4\zeta}$ are chosen to be approximately 4γ. The anisotropic patterns displayed in the Rayleigh wave map share the general
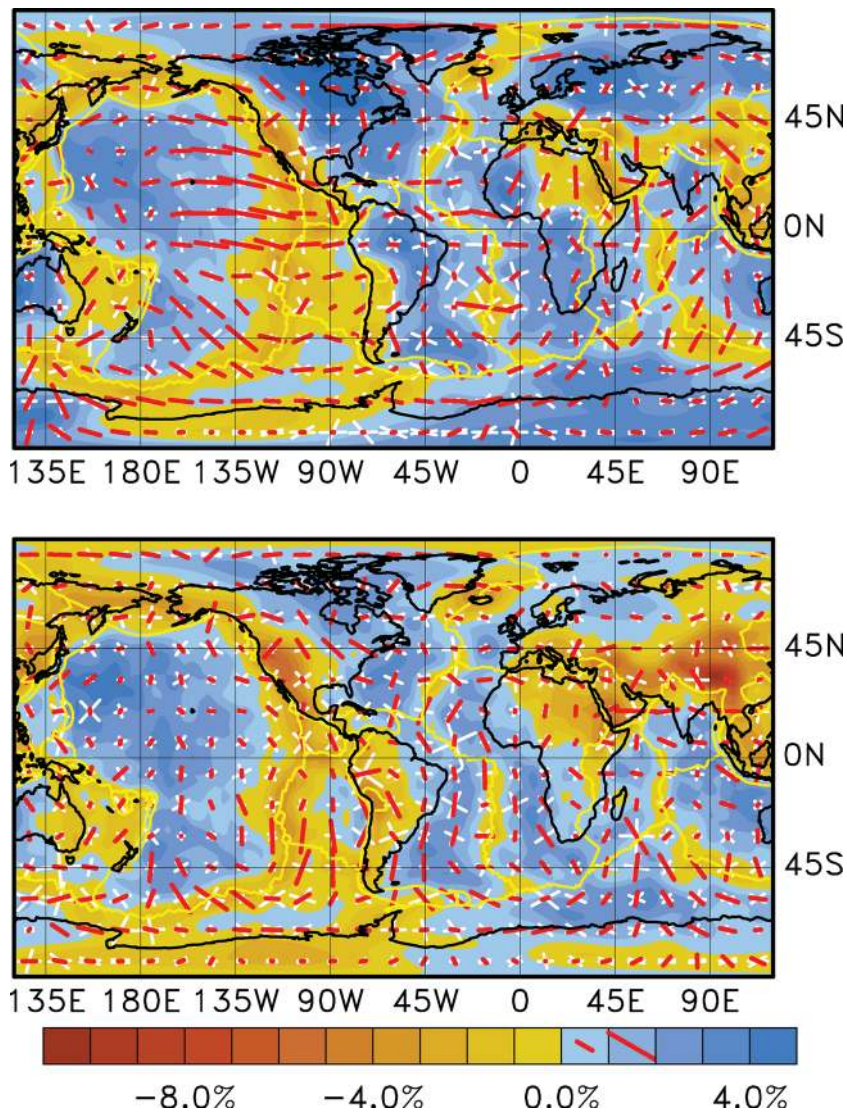
Figure 8. Anisotropic phase-velocity maps for (top) Rayleigh and (bottom) Love waves at 60 s period. The red sticks indicate the fast directions of the 2ζ anisotropic component and the white crosses indicate the two fast directions corresponding to the 4ζ component. The maximum peak-to-peak azimuthal anisotropy is 3.3 per cent for Rayleigh waves and 2.6 per cent for Love waves. The background shading shows the isotropic phase-velocity variations.

characteristics of those seen in previous studies (e.g. Montagner & Tanimoto 1990; Trampert & Woodhouse 2003). In particular, the 2ζ pattern contribution dominates, and has a broad maximum in the eastern Pacific, with fast axes in the E–W or SE–NW direction. The 4ζ pattern is much more variable in terms of orientation and amplitude, and there is no clear correlation with results of previous studies (e.g. Trampert & Woodhouse 2003). For Love waves, the amplitudes of the anisotropic parts of the models are smaller than for the Rayleigh waves, and there are no clear, large-scale patterns. Choosing values for $\gamma_{2\zeta}$ and $\gamma_{4\zeta}$ that are smaller than γ leads to unstable results. When progressively larger values for $\gamma_{2\zeta}$ and $\gamma_{4\zeta}$ are chosen, the last feature to be subdued and eventually disappear is the large-scale pattern of E–W fast directions for Rayleigh waves in the Pacific Ocean Basin.

Qualitatively, the inversion results from this experiment are similar to those of previous studies (e.g. Trampert & Woodhouse 2003). Only the 2ζ anisotropy imaged with Rayleigh waves exhibits long-wavelength, smooth anomalies. The 4ζ Rayleigh wave anomalies, and the 2ζ and 4ζ Love wave anomalies, vary over short wave-

lengths, and have an apparently random orientation and geographical distribution.

The question then arises whether any of these anisotropy results are significant or meaningful. Earlier studies have differed in their conclusions regarding the significance of anisotropic results other than the 2ζ variations for Rayleigh waves. Several authors have chosen to consider only the 2ζ anisotropy of Rayleigh waves in their studies (e.g. Nishimura & Forsyth 1988; Maggi *et al.* 2006). Trampert & Woodhouse (2003), whose data sets and techniques are similar to those used here, concluded that all types of variations except 2ζ variations for Love waves were significant, based on the observed improvement in fit and the application of a standard statistical test. Visser *et al.* (2008) arrived at a similar conclusion in their study of Love and Rayleigh wave overtones.

The improvement in data fit resulting from the introduction of anisotropic terms in the inverse problem is shown in Table 4. For the models shown in Fig. 8, the improvement in the quality-of-fit parameter is 20 per cent for the Rayleigh wave data set and 11 per cent for the Love wave data set. We have also tabulated results from

Table 4. Quality-of-fit parameters for inversions with various combinations of isotropic (0) and anisotropic (2ζ, 4ζ and 8ζ) parametrizations.

Data set		χ^2/N_r					
		0	$0 + 2\zeta$	$0 + 4\zeta$	$0 + 8\zeta$	$0 + 2\zeta + 4\zeta$	$0 + 2\zeta + 8\zeta$
L	60	2.76	2.59	2.56	2.53	2.47	2.42
R	60	2.19	1.81	1.89	1.94	1.75	1.73

inversions where only 2ζ or 4ζ variations were allowed, keeping the damping parameters the same. The greatest improvement in fit resulting from the addition of a single azimuthal term is obtained for the Rayleigh wave data set, for which the fit improves by 17 per cent when the 2ζ terms are added. However, the addition of any single azimuthal variation improves the fit to either data set by 6 per cent or more which, owing to the large number of data, is statistically significant at a high level of confidence, using standard statistical assumptions.

There exist, however, reasons to question the real significance of the observed improvement in fit. We have included in Table 4 the results for a set of additional inversions in which $\sin 8\zeta$ and $\cos 8\zeta$ azimuthal variations were allowed. There is no simple physical basis for such variations, and no reason to expect such variations to occur in the real Earth, but they allow the same level of freedom in the inversions as do the inclusions of 2ζ or 4ζ azimuthal variations. For the Love wave data set, the 8ζ anisotropy leads to a greater improvement in fit than does the 4ζ anisotropy, both when it is the only azimuthal variation allowed, and in combination with a 2ζ variation. For the Rayleigh wave data set, inclusion of 8ζ variations provides similar improvements in fit to the inclusion of 4ζ terms. The lack of a clear difference in the improvement in fit resulting from inversions with the physically plausible 2ζ and 4ζ variations and those including the implausible 8ζ variations suggests that criteria other than fit are needed in evaluating whether the inversion results are meaningful.

4.6.1 Isotropic–anisotropic trade-offs

One of the difficulties in assessing the trade-off between isotropic and anisotropic structures in the inversions is that regularization typically is needed to smooth or damp both the isotropic and anisotropic structures. As a consequence, the resulting models will naturally evolve in the direction dictated by the regularization constraints as new variables are introduced in the inverse problem. However, with the data sets of intermediate-period Rayleigh waves assembled here, no damping of the isotropic structure is strictly necessary even with the high-resolution set of basis functions. This allows us to examine the impact that adding anisotropic structure has on the isotropic structure when no preference for smoothness of the isotropic structure has been imposed through the addition of regularization.

Two characteristics that can be investigated to assess the plausibility of the anisotropic results are (1) whether the introduction of anisotropic parameters influences the retrieved isotropic structure in a way that makes it more plausible and (2) whether the retrieved anisotropic structure can be interpreted using likely physical mechanisms.

The top panels of Fig. 9 show the isotropic inversion results for Rayleigh waves at 75 s with the preferred isotropic damping parameter (as in Table 3) as well as with no damping ($\gamma = 0$). The models are very similar, and the most notable unexpected feature in the maps is the short-wavelength ripple or streak crossing the Pacific

from the northeast to the southwest. This ripple is a stable feature of all high-resolution isotropic inversions of Rayleigh waves between 50 and 100 s period that we have conducted, and it only disappears when a large value for the damping parameter γ is used. The bottom panels of Fig. 9 show the results from inversions in which a 2ζ anisotropic variation is included. The isotropic damping is as in the top panels, and the anisotropic damping is chosen as before ($\gamma_{2\zeta} = 4\gamma$). For clarity, the anisotropic part is omitted from the map in the bottom right panel. The isotropic velocity ripple disappears in both cases and instead the isotropic velocity anomalies display a smooth increase from east to west, consistent with the pattern expected based on increasing lithospheric age and cooling of the lithosphere (e.g. Stein & Stein 1992). Since no regularization of the isotropic structure was applied in the inversions on the right, the smoother structure in the bottom panel results directly from the inclusion of the anisotropic terms.

The 2ζ anisotropic pattern obtained in the inversions is characterized by a strong, large-scale anomaly associated with the younger, eastern half of the Pacific Plate. The orientations of the fast directions are not uniform, but largely in agreement with fossil spreading directions or absolute-plate-motion directions. This result is qualitatively similar to those of earlier studies (e.g. Forsyth 1975; Nishimura & Forsyth 1988; Maggi *et al.* 2006), and has been interpreted in terms of the anisotropy caused by lattice-preferred orientation of olivine resulting from current and past mantle flow and strain (e.g. Nishimura & Forsyth 1989; Gaboret *et al.* 2003; Becker *et al.* 2003).

The introduction of 2ζ anisotropy in the inversion for Rayleigh wave slowness variations produces isotropic variations that are in better agreement with patterns predicted based on a lithospheric-cooling model of the oceanic lithosphere. In addition, the anisotropic heterogeneities agree qualitatively with the olivine fabric predicted to exist in the deformed lithosphere and asthenosphere beneath the Pacific Plate. These results, in addition to the significant gain in data fit resulting from the inclusion of 2ζ anisotropy for Rayleigh waves, lead us to believe that the 2ζ results are meaningful. The introduction of 4ζ anisotropy for Rayleigh waves, or any kind of azimuthal anisotropy for Love waves, does not lead to as large improvements in fit, and does not produce models that are readily interpreted in terms of physically plausible mechanisms or that are consistent with geodynamic predictions. In our preferred models, we therefore permit only the 2ζ contributions to Rayleigh wave slowness. The dominant role of the 2ζ variations of Rayleigh waves is predicted by petrological studies (e.g. Montagner & Nataf 1986; Montagner & Anderson 1989). There is no reason to believe that the other components of anisotropy are absent in the Earth, but we are not able to constrain these components on a global scale with the data and methods employed here.

5 DISPERSION MODELS

In this step of the analysis, we use the phase-anomaly data sets to determine dispersion models for Love and Rayleigh waves. The distinction we make here between a collection of phase-slowness maps and a dispersion model is that a dispersion model can be used to evaluate the phase slowness, and its frequency derivative, at arbitrary frequencies. This property is useful for the calculation of group-slowness variations, for example. Based on our results from the inversions of phase slowness, we parametrize the Rayleigh wave phase slowness with isotropic variations and 2ζ anisotropic variations, and Love waves with only isotropic variations. Generalizing
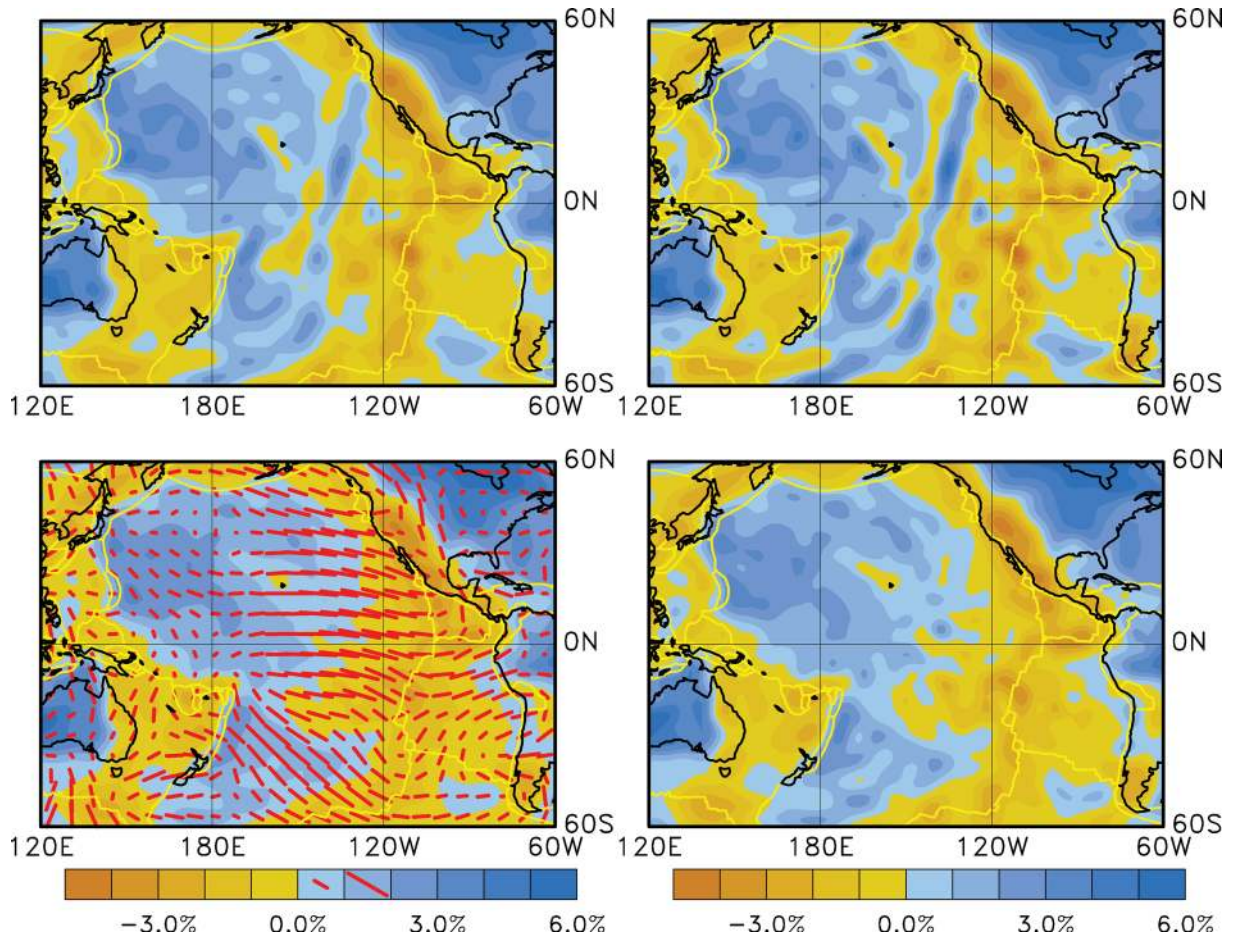
Figure 9. Maps of Rayleigh wave phase velocities in the Pacific at 75 s obtained using a global basis of 1442 spherical splines. Top left panel shows the map corresponding to the preferred damped isotropic inversion (Table 3). Bottom left panel shows map with the same isotropic damping as the map above, but including 2ζ anisotropic variations in the inversion. Top right panel shows the map resulting from an undamped isotropic inversion. Bottom right panel shows the isotropic part of the model resulting from an inversion that also includes 2ζ variations. The anisotropic part (not shown) is indistinguishable from the results on the left. In both the damped and undamped inversions, the isotropic velocity patterns in the Pacific become simpler and smoother after inclusion of anisotropic variations. The anisotropic part of the model is shown by the sticks indicating fast directions.

eq. (20) to include frequency variations, we write for the absolute phase-slowness perturbation

$$\delta p^\star(\theta, \varphi, \omega, \zeta) = \sum_{j=1}^{M} B_j(\omega) \sum_{i=1}^{N} \left[u_{ij} f_i(\theta, \varphi) \right.$$
$$\left. + a_{ij} f_i(\theta, \varphi) \, \cos 2\zeta_i + b_{ij} f_i(\theta, \varphi) \, \sin 2\zeta_i \right], \quad (31)$$

where $B_j(\omega)$ are a set of M B-spline basis functions spanning the period range 25–250 s. The total number of parameters to estimate is thus $N \times M$ for Love waves and $3N \times M$ for Rayleigh waves.

From the phase-slowness perturbation, the group-slowness perturbation $\delta g^\star(\theta, \varphi, \omega, \zeta)$ is easily calculated. We write

$$\delta g^\star(\theta, \varphi, \omega, \zeta) = \delta p^\star(\theta, \varphi, \omega, \zeta) + \omega \sum_{j=1}^{M} \frac{dB_j}{d\omega}(\omega) \sum_{i=1}^{N} \left[u_{ij} f_i(\theta, \varphi) \right.$$
$$\left. + a_{ij} f_i(\theta, \varphi) \, \cos 2\zeta_i + b_{ij} f_i(\theta, \varphi) \, \sin 2\zeta_i \right]. \quad (32)$$

We use the same 1442-node spherical-spline basis as previously to parametrize the dispersion model in the horizontal dimension; we use 12 unevenly spaced B-splines to describe the frequency
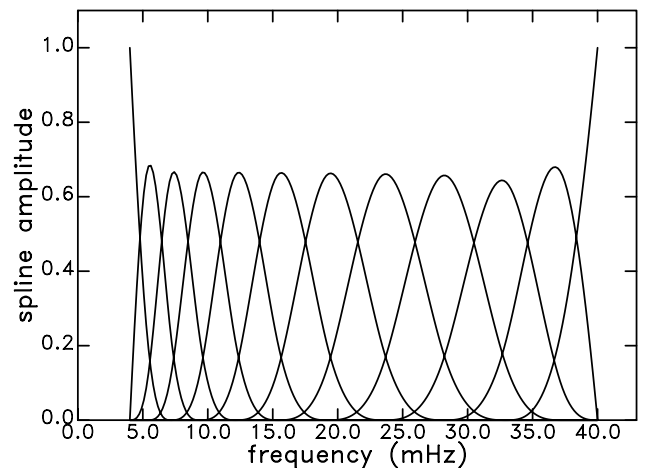

Figure 10. Spline functions used to parametrize the dispersion model with respect to frequency.

variations (Fig. 10). The two data sets used to constrain the coefficients u_{ij}, a_{ij} and b_{ij} are the approximately 750,000 Love wave and 2.75 million Rayleigh wave phase-anomaly observations. We form the data-misfit portion of $\tilde{\chi}^2$ as in eq. (22). The problem

requires regularization, and we choose to minimize the lateral roughness of phase and group slowness. For phase slowness, we write

$$\mathcal{R}_P = \left[\int_4^{40} W(f) \frac{1}{4\pi} \int_\Omega (\nabla \delta p) \cdot (\nabla \delta p) \, d\Omega \, df \right]^{1/2}, \qquad (33)$$

where the first integral is from 4 to 40 mHz and $W(f)$ is a function that is chosen to equalize the contributions at different frequencies, since slowness variations are larger at shorter periods. Similarly, for group slowness, we write

$$\mathcal{R}_G = \left[\int_4^{40} W(f) \frac{1}{4\pi} \int_\Omega (\nabla \delta g) \cdot (\nabla \delta g) \, d\Omega \, df \right]^{1/2}, \qquad (34)$$

where $W(f)$ is the same weighting function. The function to minimize is then

$$\tilde{\chi}^2 = \left(\chi^2 + \gamma_P \mathcal{R}_P^2 + \gamma_G \mathcal{R}_G^2 \right), \qquad (35)$$

where γ_P and γ_G are regularization parameters that need to be chosen.

The horizontal roughness of the slowness is effectively controlled by the γ_P parameter, which we choose so that the dispersion model predicts slowness maps at the observed periods of similar roughness to those derived at individual periods. With phase-anomaly data from 15 different periods and only 12 spline functions describing the variations over frequency, the dispersion-model inversion is overdetermined, and, with $\gamma_G = 0$ yields results similar to those of a spline interpolation of the phase-slowness models at different periods. However, such interpolated models predict group-slowness maps that are rough and unrealistic. This is not surprising, since

group slowness is highly sensitive to the frequency derivative of phase slowness. The purpose of introducing the damping parameter γ_G is thus to smooth the frequency variations of phase slowness in a realistic manner by requiring the lateral variations of group slowness to be smooth.

5.1 Love waves

In our preferred inversion for the Love wave portion of the dispersion model, we chose $\gamma_P = 4\gamma_G$ and the weighting function $W(f)$ is

$$W(f) = \frac{1}{f}. \qquad (36)$$

The factor of four difference in the damping of phase- and group-slowness variations compensates for the approximately factor-of-two greater rms signal of the group slowness at a given period, and $W(f)$ compensates for the nearly order-of-magnitude range in slowness variations between 4 and 40 mHz. These choices result in a dispersion model that predicts phase-velocity maps with very similar characteristics to those obtained in the period-specific inversions. Correlation coefficients between the phase-velocity maps predicted by the dispersion model and those inverted directly are larger than 0.98 at all periods, and the rms and roughness parameters differ by less than 10 per cent. Phase-velocity maps derived from the preferred Love wave dispersion model, which we refer to as GDM52L, are shown in Fig. 11. Strength, roughness and quality-of-fit parameters for GDM52L are given in Table 3.
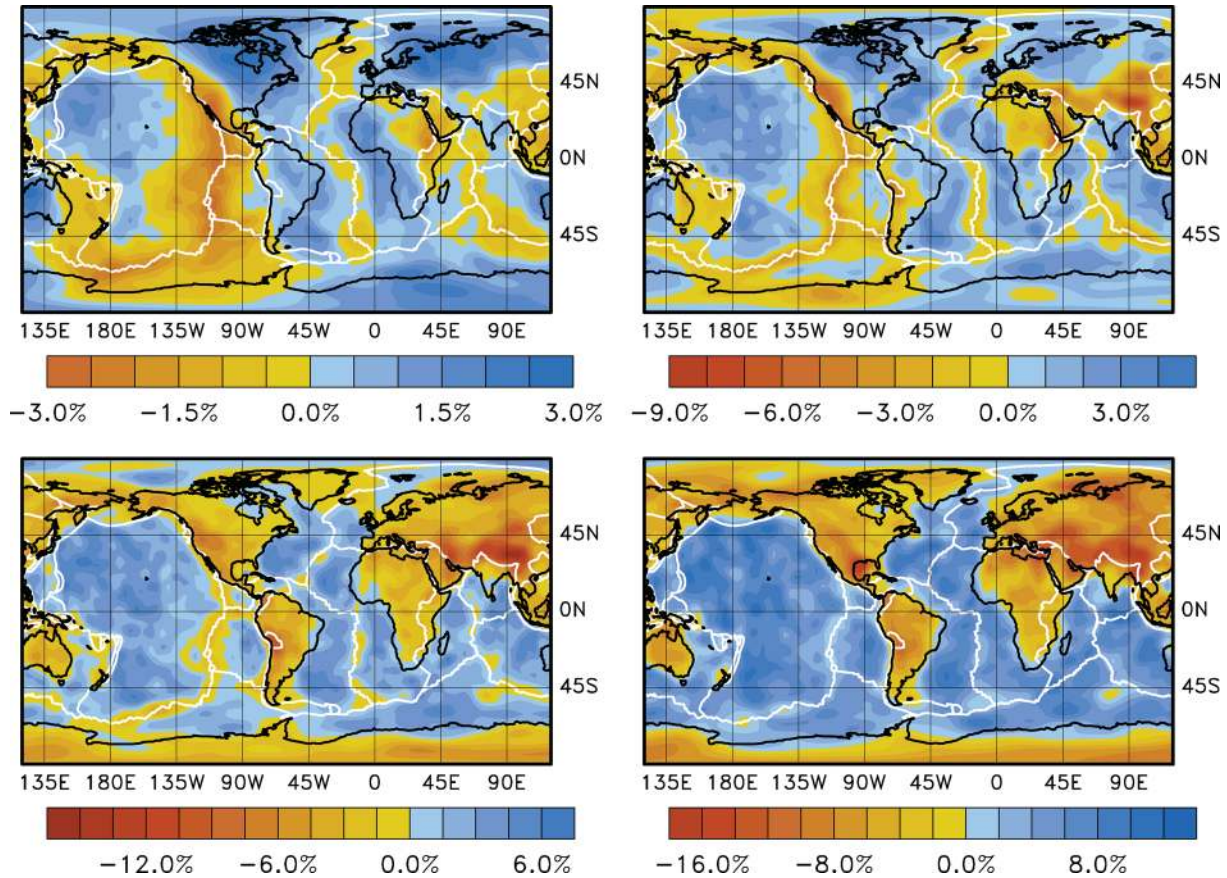

Figure 11. Phase-velocity maps for Love waves at different periods evaluated from the Love wave dispersion model GDM52: top left, 250 s; top right, 75 s; bottom left, 40 s and bottom right, 25 s. Note the different scales. All deviations are with respect to PREM predictions.
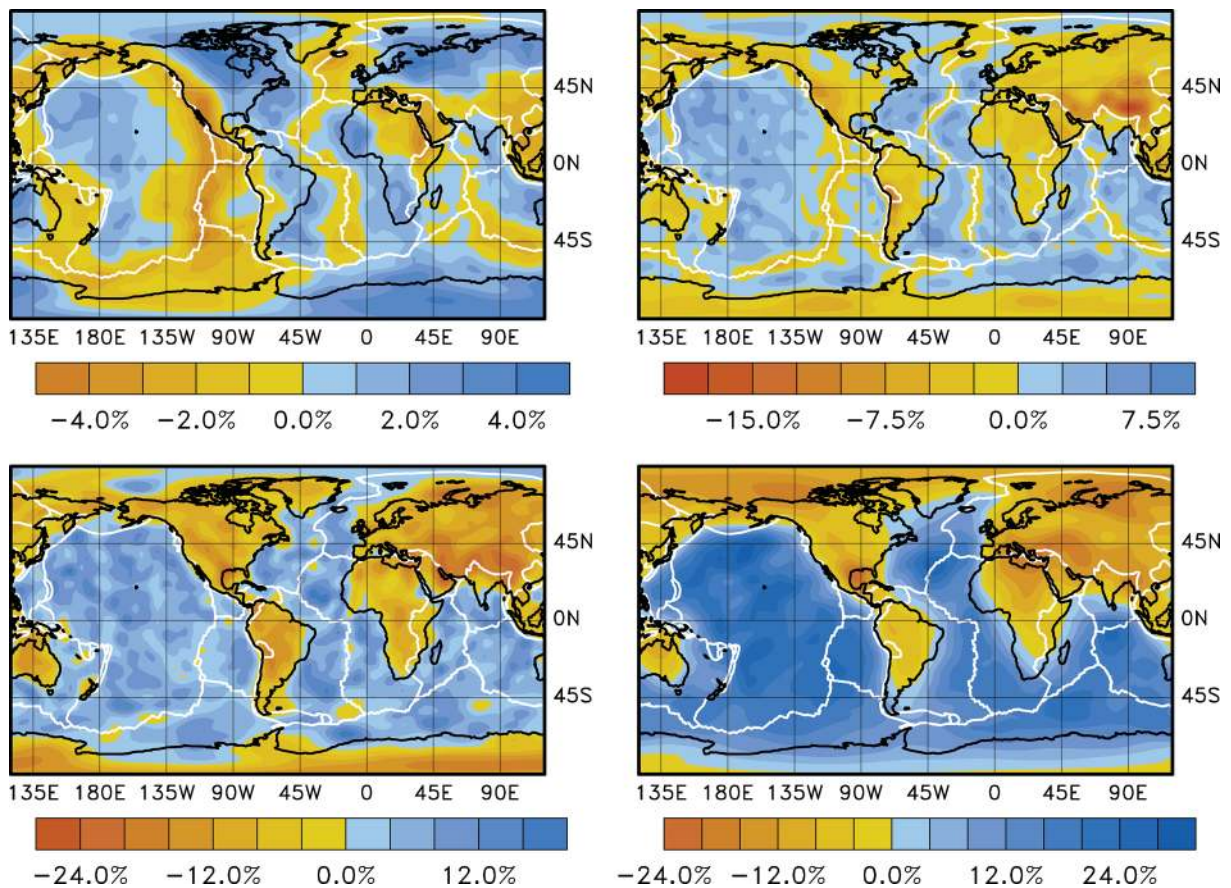
Figure 12. Group-velocity maps for Love waves at different periods evaluated from the Love wave dispersion model GDM52L: top left, 250 s; top right, 75 s; bottom left, 40 s and bottom right, 25 s. Note the different scales. All deviations are with respect to PREM predictions.

Group-velocity maps predicted from GDM52L at four periods are shown in Fig. 12. At 25 s, the group-velocity map exhibits very large variations (−23 to +31 per cent). Although the map is very smooth, the slowest velocities appear to be spatially correlated with known regions of very thick sediments: the Gulf of Mexico, the Barents Sea and the Black Sea. The very high velocities in some areas of the oceans are probably spurious and the consequence of poor station coverage. With lower damping (γ_G), the short-period group-velocity maps rapidly become unstable. At 40-s period, the range of anomalies is similar, but the extreme values are more localized. The slowest anomaly (−25 per cent) is associated with the Gulf of Mexico. The group-velocity maps at longer periods (75 and 250 s in Fig. 12) display patterns that are also seen in phase-velocity maps, although shifted in period; the 75 s group-velocity map is correlated very well (0.98) with the phase-velocity map at 50 s, and the 250-s map is very well correlated with the phase-velocity map at 150 s (0.98). This pattern of correlations reflects the different sensitivities of group and phase velocity to radial Earth structure.

Few global tomographic maps of Love wave group velocity have been published. Larson & Ekström (2001) derived isotropic Love and Rayleigh wave group-velocity maps between 35 and 175 s from group-velocity measurements based on dispersion curves of the same kind analyzed here. We calculate the spatial correlation of group-velocity maps derived from GDM52L at 35, 50, 100 and 150 s, with the corresponding maps from Larson & Ekström (2001). The correlation is greater than 0.80 at all four periods, reflecting good agreement. The new maps are marginally rougher and visually

they appear to have more sharply defined anomalies, such as mid-ocean ridges and cratonic roots.

5.2 Rayleigh waves

In our preferred Rayleigh wave inversion, we chose the same relative damping for the phase and group slowness as in the Love wave inversion, $\gamma_P = 4\gamma_G$, and the same weighting function $W(f)$. We used a damping parameter for the azimuthal anisotropy that yields results similar to those obtained in the single-frequency inversions. We refer to the preferred Rayleigh wave dispersion model as GDM52R; strength, roughness and quality-of-fit parameters for GDM52R are given in Table 3.

Fig. 13 shows phase-velocity maps evaluated from GDM52R at four periods. The variations in isotropic velocity display a striking correlation with the distribution of continents and oceans at 25 s period, and a pattern that is distinctly uncorrelated with surface geology and tectonics at 250 s. The 2ζ anisotropic variations vary in strength at different periods, but the patterns are similar for the maps at 25, 40 and 75 s period.

The isotropic parts of the group-velocity maps calculated from GDM52R are shown in Fig. 14. Mapped variations at 25 s are very large (−30 to +18 per cent), and strongly correlated with the distribution of continents and oceans. As with the Love wave maps, the longer period isotropic components of the Rayleigh wave group-velocity maps show similar patterns to those exhibited by the phase-velocity maps, although shifted in period: the group-velocity map at 40 s is best correlated with the 25-s phase-velocity map (0.97),
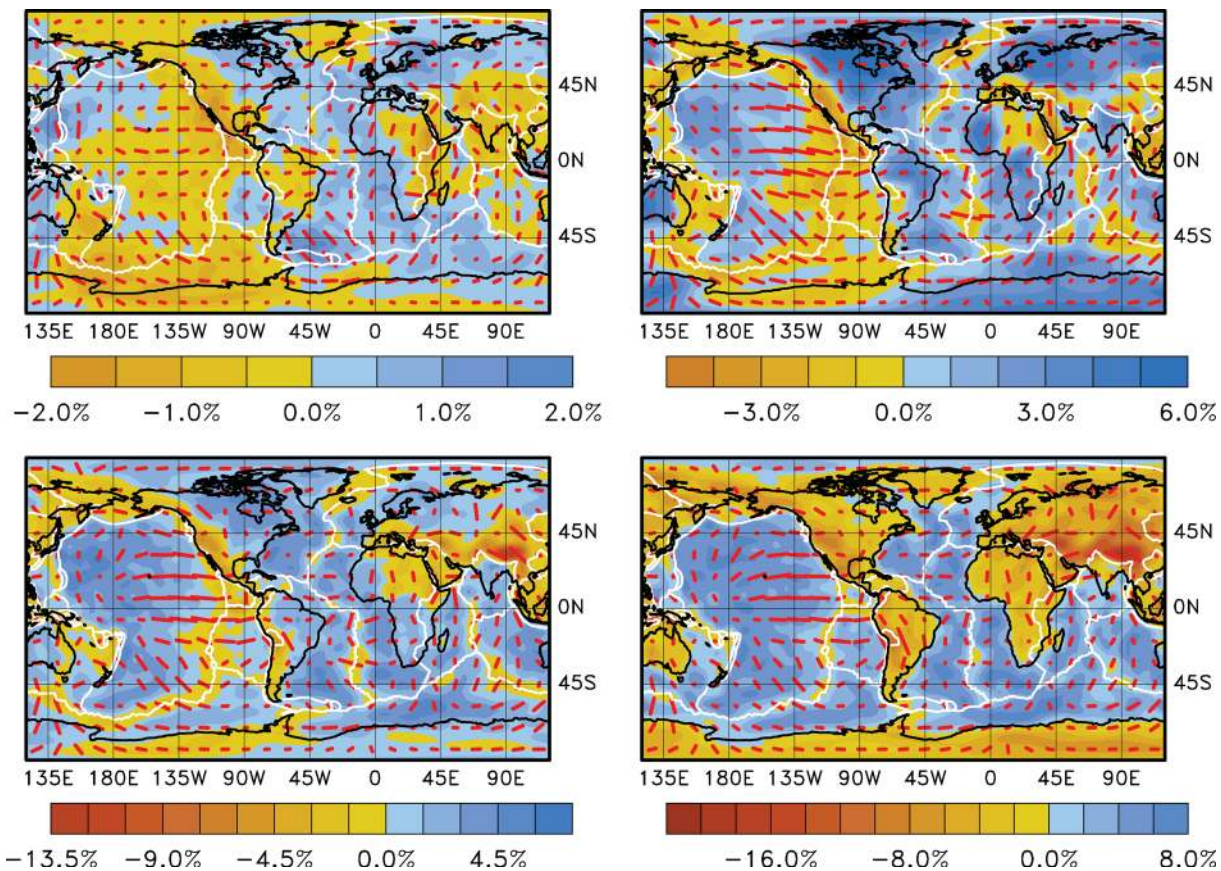
Figure 13. Phase-velocity maps for Rayleigh waves at different periods evaluated from the Rayleigh wave dispersion model GDM52R: top left, 250 s; top right, 75 s; bottom left, 40 s and bottom right, 25 s. Note the different scales for the isotropic velocity variations. All deviations are with respect to PREM predictions. The anisotropic fast directions are indicated with the red sticks, and the scale of the sticks is the same in all maps. The longest stick corresponds to a peak-to-peak anisotropy of 2.6 per cent.

the 75-s map with the 50-s phase-velocity map (0.98) and the 250-s map with the 150-s phase-velocity map (0.93).

The correlation of the new group-velocity maps with the group-velocity maps of Larson & Ekström (2001) is 0.87 at 35 s, but significantly less at longer periods: 0.75 at 50 s, 0.57 at 100 s and 0.64 at 150 s. The worse correlation at longer periods is likely a consequence of the lack of consideration of azimuthal anisotropy in the Larson & Ekström (2001) study. The intermediate-period maps of Larson & Ekström (2001) exhibit similar streaks in the Pacific Ocean to those described earlier as resulting from the neglect of anisotropic terms. In fact, Larson & Ekström (2001) comment on the possibility that these features are the result of modelling an anisotropic structure with an isotropic model.

6 DISCUSSION

The main result of this study is the surface wave dispersion model GDM52, consisting of the isotropic Love wave model GDM52L and the anisotropic Rayleigh wave model GDM52R. The model provides global average and local constraints on elastic Earth structure, and can be used to calculate path-specific surface wave dispersion between two arbitrary locations on the Earth.

The average phase and group velocities of the Earth in the range 25–250 s are well constrained in this study. Fig. 15 shows the deviations of average Rayleigh and Love wave phase velocities from PREM. As also pointed out in ETL97, PREM underestimates phase velocities of Rayleigh waves around 50 s period, probably as a con-

sequence of a too-strong global average radial anisotropy in the PREM lithosphere. In this study, we also find that Love wave phase velocities are too slow in PREM at short periods. This may indicate that the PREM average crust is too thin. The deviations of the observed dispersion from that predicted by PREM is also evident in the global average group velocities (Fig. 16). Observed Rayleigh wave group velocities are faster than PREM by 1–2 per cent at 40–100 s period, and slower than PREM at shorter periods. Love wave group velocities deviate from PREM predictions mainly at short periods, where they are as much as 5 per cent faster at 25 s period.

The horizontal separation of spherical-spline knots in GDM52, approximately 650 km, establishes the shortest length scale over which the model can represent a sharp contrast in dispersion. The close correspondence of continent–ocean boundaries with rapid changes in phase and group velocity (Figs 11–14) suggests that in many areas, the nominal resolution is nearly achieved, especially at shorter periods. The continent–continent plate boundary separating Eurasia from India is also very distinct in both Love and Rayleigh wave dispersion over a broad range of periods. Fig. 17 illustrates the difference in local dispersion in central Tibet (32°N, 90°E) and central India (20°N, 78°E).

For Rayleigh waves, GDM52 describes anisotropic propagation characteristics, and the 2ζ variations of Rayleigh wave phase velocities are shown in map view in Fig. 13. A broad maximum in the strength of anisotropy is associated with the eastern portion of the Pacific Plate, with fast directions primarily in the east–west and southeast–northwest directions. The patterns at short and
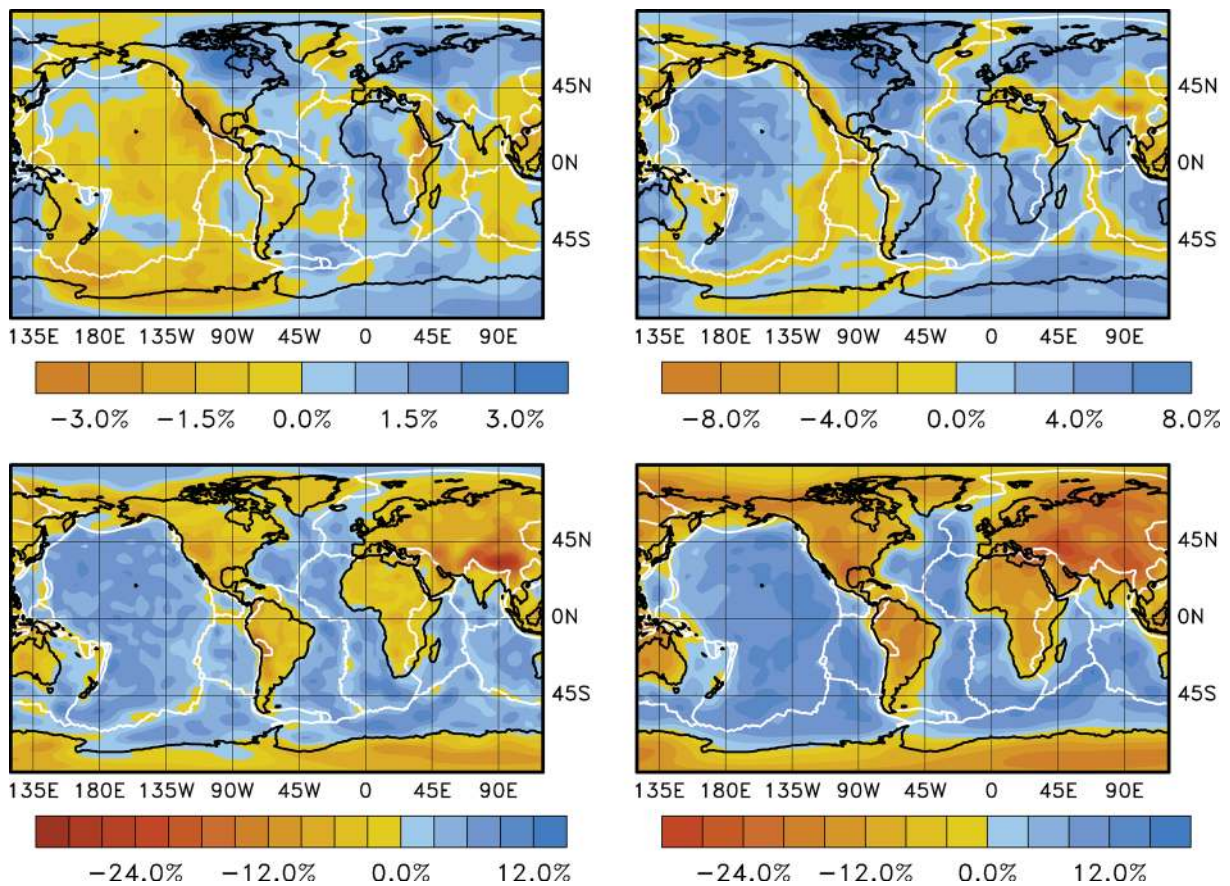
Figure 14. Group-velocity maps for Rayleigh waves at different periods evaluated from the Rayleigh wave dispersion model GDM52R: top left, 250 s; top right, 75 s; bottom left, 40 s and bottom right, 25 s. Note the different scales. All deviations are with respect to PREM predictions.
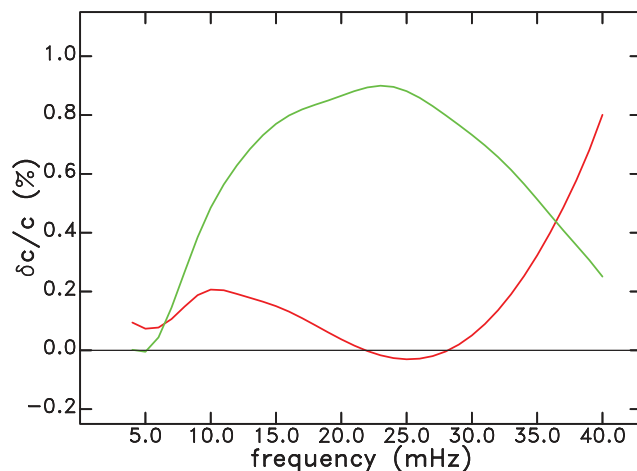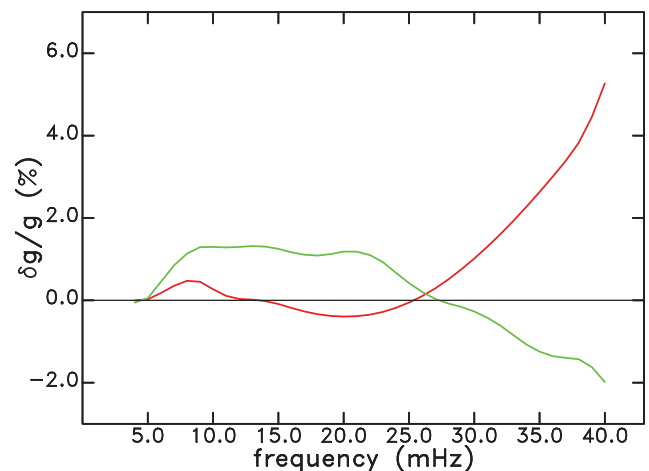

Figure 15. Global average phase-velocity variations from GDM52 for (red) Love and (green) Rayleigh waves, with respect to the PREM model.

Figure 16. Global average group-velocity variations from GDM52 for (red) Love and (green) Rayleigh waves, with respect to the PREM model.

intermediate periods show strong correlation, with the map at 250 s displaying less coherent patterns and a less pronounced strength maximum associated with the Pacific Plate. Variations of strength and direction of surface wave azimuthal anisotropy with wave period result from the distribution of intrinsic anisotropy and variations in the depth sensitivity to anisotropy. Observations therefore have the potential to constrain the current or past mechanisms giving rise to the anisotropic fabrics. Fig. 18 shows the strength (peak-to-peak) and fast direction of anisotropy at three different locations in the

Pacific Basin as a function of frequency. The variation in the northeastern Pacific (35°N, 135°W, red line in Fig. 18) shows a maximum strength at around 75 s period, and a fast azimuth that rotates from 110° at 100 s to 92° at 25 s. In the southern Pacific (35°S, 135°W, green line), the strength of anisotropy is less, and the rotation follows a different trend, from 135° at 100 s to 150° at 25 s. For a point in the middle of the Nazca Plate (15°S, 90°W), the maximum anisotropy occurs at 40 s, and the fast azimuth rotates from 60° at 100 s to 85° at 25 s. Although the fast directions for the northern
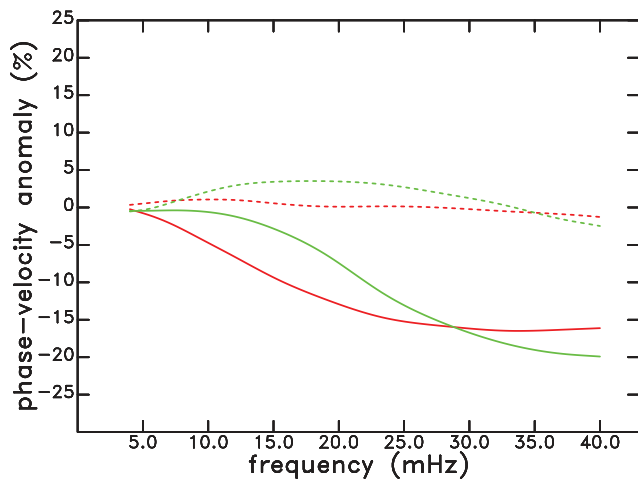
Figure 17. Isotropic phase-velocity dispersion across the India–Eurasia plate boundary. Solid lines give the local (red) Love and (green) Rayleigh wave dispersion calculated for a point in Tibet (32°N, 90°E). Dashed lines give the local dispersion for a point in central India (20°N, 78°E).
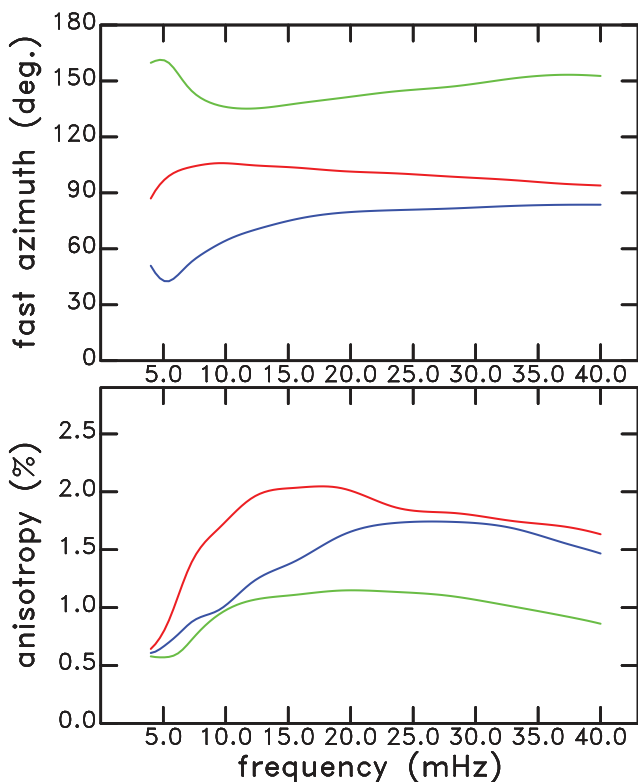

Figure 18. Strength and fast direction of 2ζ anisotropy at three locations in the Pacific Basin evaluated from the Rayleigh wave dispersion model GDM52R: 35°N, 135°W (red), 35°S, 135°W (green) and 15°S, 90°W (blue). The azimuths are clockwise with respect to North and the strength is given as the peak-to-peak value.

point are in qualitative agreement with both the absolute motion of the Pacific Plate and the fossil spreading direction, the fast directions at the southern point clearly deviate strongly at all periods from the nearly east–west spreading direction, perhaps suggesting a more complicated relationship to past and current plate motions.

An important use for tomographic models of the Earth is the prediction of wave propagation, primarily traveltimes, between arbitrary source locations and seismic stations. For body waves, the
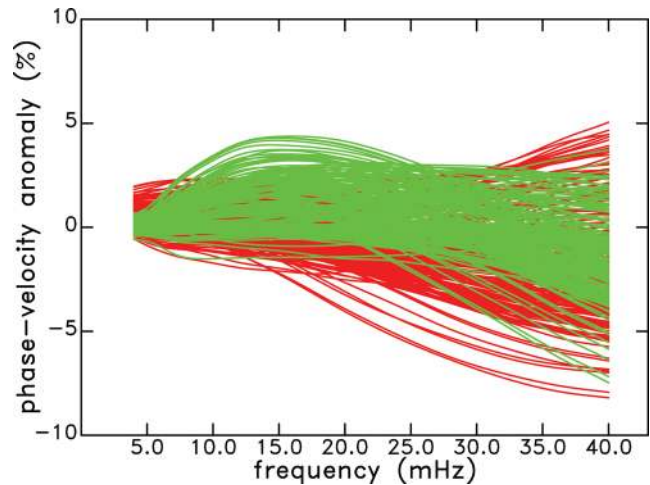

Figure 19. Dispersion curves calculated from GDM52 for (red) Love and (green) Rayleigh waves for paths originating at Helheim Glacier, Greenland (66°N, 38°W) to the 194 stations on Fig. 2 located at a distance less than 90° from Helheim Glacier.

improved ability to account for propagation delays can result in more accurate and precise determinations of earthquake hypocentres. For surface waves, a more accurate prediction of frequency-dependent propagation delays can allow the remaining surface wave phase to be interpreted in terms of source phase, and thereby the source mechanism. In addition, since propagation-phase delays at short periods can amount to several cycles (Fig. 3), corrections for propagation phase are very important for any analysis that relies on signal enhancement by phase-coherent stacking of surface wave phases. For example, in their development and application of a long-period event detector based on surface waves, Ekström *et al.* (2003) and Ekström (2006a) found that application of propagation-phase corrections greatly improved the detection and location of seismic sources in the period band 35–150 s. Fig. 19 illustrates the variability of dispersion predicted by GDM52 from Helheim Glacier in Greenland, a source area of so-called glacial earthquakes (Ekström *et al.* 2003; Nettles *et al.* 2008). Because of their spectral characteristics, these earthquakes are best detected and located using surface waves. Dispersion curves to existing seismic stations within 90° are shown, illustrating the wide range of propagation characteristics that need to be accounted for in the analysis of events from this site. No earthquakes from this region were used in the determination of the GDM52 model.

The dispersion model GDM52 was derived using ray theory, and it is therefore most suitable for making predictions using the same theory. Though not pursued here, the phase-anomaly data collected and developed in this study could alternatively be investigated using other wave-propagation theories. To facilitate further analyses of the model and the data, the phase-anomaly data set, the model coefficients for GDM52 and programs to evaluate the dispersion model at arbitrary periods and locations are available at www.ldeo.columbia.edu/~ekstrom.

REFERENCES

Arvidsson, R. & Ekström, G., 1998. Global CMT analysis of moderate earthquakes, $M_w \geqslant 4.5$, using intermediate-period surface waves, *Bull. seism. Soc. Am.,* **88**(4), 1003–1013.

Becker, T.W., Kellogg, J.B., Ekström, G. & O'Connell, R.J., 2003. Comparison of azimuthal seismic anisotropy from surface waves and finite strain from global mantle-circulation models, *Geophys. J. Int.,* **155**(2), 696–714.

Becker, T.W., Ekström, G., Boschi, L. & Woodhouse, J.H., 2007. Length scales, patterns and origin of azimuthal seismic anisotropy in the upper mantle as mapped by Rayleigh waves, *Geophys. J. Int.,* **171,** 451–462.

Beucler, É. & Montagner, J.-P., 2006. Computation of large anisotropic seismic heterogeneities (CLASH), *Geophys. J. Int.,* **165,** 447–468.

Bird, P., 2003. An updated digital model of plate boundaries, *Geochem. Geophys. Geosyst.,* **4**(3), 1027, doi:10.1029/2001GC000252.

Boschi, L., 2006. Global multiresolution models of surface wave propagation: comparing equivalently regularized born and ray theoretical solutions, *Geophys. J. Int.,* **167,** 238–252.

Dahlen, F.A., Hung, S.-H. & Nolet, G., 2000. Fréchet kernels for finite-frequency traveltimes-1. Theory, *Geophys. J. Int.,* **141,** 157–174.

Debayle, É., Kennett, B.L.N. & Priestley, K., 2005. Global azimuthal seismic anisotropy and the unique plate-motion deformation of Australia, *Nature,* **433,** 509–512.

Dziewonski, A.M. & Anderson, D.L., 1981. Preliminary reference Earth model, *Phys. Earth Planet. Int.,* **25,** 297–356.

Dziewonski, A.M., Chou, T.-A. & Woodhouse, J.H., 1981. Determination of earthquake source parameters from waveform data for studies of global and regional seismicity, *J. geophys. Res.,* **86,** 2825–2852.

Ekström, G., 2000. Mapping the lithosphere and asthenosphere with surface waves: lateral structure and anisotropy, *Geophys. Monogr. Ser.,* **121,** 239–255.

Ekström, G., 2006a. Global detection and location of seismic sources by using surface waves, *Bull. seism. Soc. Am.,* **96**(4A), 1201–1212.

Ekström, G., 2006b. A simple method of representing azimuthal anisotropy on a sphere, *Geophys. J. Int.,* **165,** 668–671.

Ekström, G., Tromp, J. & Larson, E.W.F., 1997. Measurements and global models of surface wave propagation, *J. geophys. Res.,* **102,** 8137–8157.

Ekström, G., Nettles, M. & Abers, G.A., 2003. Glacial earthquakes, *Science,* **302**(5645), 622–624.

Ekström, G., Dziewonski, A.M., Maternovskaya, N.N. & Nettles, M., 2005. Global seismicity of 2003: centroid-moment-tensor solutions for 1087 earthquakes, *Phys. Earth planet. Inter.,* **148,** 327–351.

Engdahl, E.R., Dewey, J.W. & Fujita, K., 1982. Earthquake location in island arcs, *Phys. Earth Planet. Inter.,* **30**(2–3), 145–156.

Forsyth, D.W., 1975. The early structural evolution and anisotropy of the oceanic upper mantle, *Geophys. J. R. astr. Soc.,* **43,** 103–162.

Gaboret, C., Forte, A.M. & Montagner, J.-P., 2003. The unique dynamics of the Pacific Hemisphere mantle and its signature on seismic anisotropy, *Earth planet. Sci. Lett.,* **208**(3–4), 219–233.

van Heijst, H.J. & Woodhouse, J.H., 1999. Global high-resolution phase velocity distributions of overtone and fundamental-mode surface waves determined by mode branch stripping, *Geophys. J. Int.,* **137,** 601–620.

Larson, E.W.F. & Ekström, G., 2001. Global models of surface wave group velocity, *Pure appl. Geophys.,* **158,** 1377–1399.

Laske, G. & Masters, G., 1996. Constraints on global phase velocity maps from long-period polarization data, *J. geophys. Res.,* **101,** 16 059–16 075.

Maggi, A., Debayle, É., Priestley, K. & Barruol, G., 2006. Azimuthal anisotropy of the Pacific region, *Earth planet. Sci. Lett.,* **250,** 53–71.

Masters, G., Jordan, T.H., Silver, P.G. & Gilbert, F., 1982. Aspherical Earth structure from fundamental spheroidal mode data, *Nature,* **298,** 609–613.

Montagner, J.-P. & Anderson, D.L., 1989. Petrological constraints on seismic anisotropy, *Phys. Earth planet. Inter.,* **54,** 82–105.

Montagner, J.-P. & Guillot, L., 2000. Seismic anisotropy in the Earth's mantle, *Problems in Geophysics for the New Millenium,* pp. 217–253, eds Boschi, E., Ekström, G. & Morelli, A., Editrice Compositori, Bologna, Italy.

Montagner, J.-P. & Jobert, N., 1988. Vectorial tomography—II. Application to the Indian Ocean, *Geophys. J. R. astr. Soc.,* **94**(2), 309–344.

Montagner, J.-P. & Nataf, H.-C., 1986. A simple method for inverting the azimuthal anisotropy of surface waves, *J. geophys. Res.,* **91**(B1), 511–520.

Montagner, J.-P. & Tanimoto, T., 1990. Global anisotropy in the upper mantle inferred from the regionalization of phase velocities, *J. geophys. Res.,* **95,** 4797–4819.

Montagner, J.-P. & Tanimoto, T., 1991. Global upper mantle tomography of seismic velocities and anisotropies, *J. geophys. Res.,* **96,** 20 337–20 351.

Nakanishi, I. & Anderson, D.L., 1982. World-wide distribution of group velocity of mantle Rayleigh waves as determined by spherical harmonic inversion, *Bull. seism. Soc. Am.,* **72,** 1185–1194.

Nakanishi, I. & Anderson, D.L., 1983. Measurements of mantle wave velocities and inversion for lateral heterogeneity and anisotropy, 1, Analysis of great circle phase velocities, *J. geophys. Res.,* **88,** 10 267–10 283.

Nakanishi, I. & Anderson, D.L., 1984. Measurements of mantle wave velocities and inversion for lateral heterogeneity and anisotropy, 2, Analysis by the single station method, *Geophys. J. R. astr. Soc.,* **78,** 573–617.

Nataf, H.-C., Nakanishi, I. & Anderson, D.L., 1986. Measurements of mantle wave velocities and inversion for lateral heterogeneity and anisotropy, 3, Inversion, *J. geophys. Res.,* **91,** 7261–7307.

Nettles, M. *et al.*, 2008. Step-wise changes in glacier flow speed coincide with calving and glacial earthquakes at Helheim Glacier, Greenland, *Geophys. Res. Lett.,* **35,** L24503, doi:10.1029/2008GL036127.

Nishimura, C.E. & Forsyth, D.W., 1988. Rayleigh wave phase velocities in the Pacific with implications for azimuthal anisotropy and lateral heterogeneities, *Geophys. J. R. astr. Soc.,* **94**(3), 479–501.

Nishimura, C.E. & Forsyth, D.W., 1989. The anisotropic structure of the upper mantle in the Pacific, *Geophys. J. Int.,* **96**(2), 203–229.

Oliver, J., 1962. A summary of observed seismic surface wave dispersion, *Bull. seism. Soc. Am.,* **52,** 81–86.

Ritsema, J., Deuss, A., van Heijst, H.J. & Woodhouse, J.H., 2010. S40RTS: a degree-40 shear-velocity model for the mantle from new Rayleigh wave dispersion, teleseismic traveltime and normal-mode splitting function measurements, *Geophys. J. Int.*, **184,** 1223–1236, doi:10.1111/j.1365-246X.2010.04884.x.

Smith, G.P. & Ekström, G., 1996. Improving teleseismic event locations using a three-dimensional Earth model, *Bull. seism. Soc. Am.,* **86**(3), 788–796.

Smith, G.P. & Ekström, G., 1997. Interpretation of earthquake epicenters and CMT centroid locations, in terms of rupture length and direction, *Phys. Earth planet. Inter.,* **102,** 123–132.

Smith, M.L. & Dahlen, F.A., 1973. The azimuthal dependence of Love and Rayleigh wave propagation in a slightly anisotropic medium, *J. geophys. Res.,* **78,** 3321–3333.

Spetzler, J., Trampert, J. & Snieder, R., 2002. The effect of scattering in surface wave tomography, *Geophys. J. Int.,* **149,** 755–767.

Stein, C.A. & Stein, S., 1992. A model for the global variation in oceanic depth and heat flow with lithospheric age, *Nature,* **359,** 123–129.

Tanimoto, T., 1985. The Backus–Gilbert approach to the three-dimensional structure in the upper mantle: I. Lateral variation of surface-wave phase velocity with its error and resolution, *Geophys. J. Int.,* **82,** 105–123.

Tanimoto, T. & Anderson, D.L., 1984. Mapping convection in the mantle, *Geophys. Res. Lett.,* **11,** 287–290.

Tanimoto, T. & Anderson, D.L., 1985. Lateral heterogeneity and azimuthal anisotropy of the upper mantle: Love and Rayleigh waves 100–250 s, *J. geophys. Res.,* **90,** 1842–1858.

Trampert, J. & Spetzler, J., 2006. Surface wave tomography: finite-frequency effects lost in the null space, *Geophys. J. Int.,* **164,** 394–400.

Trampert, J. & Woodhouse, J.H., 1995a. Global azimuthal anisotropy inferred from surface waves, *EOS, Trans. Am. geophys. Un.,* **76,** Fall Meeting Supplement, Abstract S42C–9.

Trampert, J. & Woodhouse, J.H., 1995b. Global phase velocity maps of Love and Rayleigh waves between 40 and 150 seconds, *Geophys. J. Int.,* **122,** 675–690.

Trampert, J. & Woodhouse, J.H., 1996. High resolution global phase velocity distributions, *Geophys. Res. Lett.,* **23,** 21–24.

Trampert, J. & Woodhouse, J.H., 2003. Global anisotropic phase velocity maps for fundamental mode surface waves between 40 and 150 s, *Geophys. J. Int.,* **154,** 154–165.

Tromp, J. & Dahlen, F.A., 1992. Variational principles for surface wave propagation on a laterally heterogeneous Earth—II. Frequency-domain JWKB theory, *Geophys. J. Int.,* **109,** 599–619.

Tromp, J. & Dahlen, F.A., 1993. Maslov theory for surface wave propagation on a laterally heterogeneous Earth, *Geophys. J. Int.,* **115,** 512–528.

Visser, K., Trampert, J. & Kennett, B.L.N., 2008. Global anisotropic phase velocity maps for higher mode Love and Rayleigh waves, *Geophys. J. Int.,* **172,** 1016–1032.

Wang, Z. & Dahlen, F.A., 1995. Spherical-spline parameterization of three-dimensional Earth models, *Geophys. Res. Lett.,* **22,** 3099–3102.

Wong, Y.K., 1989. Upper mantle heterogeneity from phase amplitude data of mantle waves, *PhD thesis*, Harvard University.

Woodhouse, J.H. & Dziewonski, A.M., 1984. Mapping the upper mantle: three-dimensional modeling of Earth structure by inversion of seismic waveforms, *J. geophys. Res.,* **89,** 5953–5986.

Yang, X. et al., 2004. Validation of regional and teleseismic travel-time models by relocating ground-truth events, *Bull. seism. Soc. Am.,* **94**(3), 897–919.

Yoshizawa, K. & Kennett, B.L.N., 2002. Determination of the influence zone for surface wave paths, *Geophys. J. Int.,* **149,** 440–453.

Zhang, Y.-S. & Lay, T., 1996. Global surface wave phase velocity variations, *J. geophys. Res.,* **101,** 8415–8436.

Zhou, Y., Dahlen, F.A. & Nolet, G., 2004. Three-dimensional sensitivity kernels for surface wave observables, *Geophys. J. Int.,* **158,** 142–168.

Zhou, Y., Dahlen, F.A. & Nolet, G., 2005. Finite-frequency effects in global surface-wave tomography, *Geophys. J. Int.,* **163,** 1087–1111.